Deterministic fabrication of 3D/2D perovskite bilayer stacks for durable and efficient solar cells

Siraj Sidhik, Yafei Wang, Michael de Siena, Reza Asadpour, Andrew Torma, Tanguy Terlier, Kevin Ho, Wenbin Li, Anand Puthirath, Xinting Shuai, et al.

https://www.science.org/doi/10.1126/science.abq7652; SCIENCE 377, ISSUE 6613, PP 1425-1430 (2022) DOI: 10.1126/SCIENCE.ABQ7652

Deterministic fabrication of 3D|2D perovskite bilayer stacks for durable and efficient solar cells

Siraj Sidhik[1,2], Yafei Wang[2,3], Michael De Sienna[4], Reza Asadpour[5], Andrew Torma[6], Tanguy Terlier[7], Kevin Ho[8], Wenbin Li[2,6], Anand B. Puthirath[1], Xinting Shuai[1], Ayush Agarwal[2], Boubacar Traore[9], Matthew Jones[1,10], Rajiv Giridharagopal[8], Pulickel M. Ajayan[1], Joseph Strzalka[11], David Ginger[8], Claudine Katan[9], Muhammad Ashraful Alam[5], Jacky Even[12]*, Mercouri G. Kanatzidis[4], and Aditya D. Mohite[1,2]*

[1]Material Science and Nanoengineering, Rice University, Houston, Texas 77005, USA.

[2]Department of Chemical and Biomolecular Engineering, Rice University, Houston, Texas 77005, USA.

[3]School of Mechanical and Electric Engineering, Guangzhou University, Guangzhou, Guangdong, 510006, China.

[4]Department of Chemistry and Department of Materials Science and Engineering, Northwestern University, Evanston, Illinois 60208, USA.

[5]School of Electrical and Computer Engineering, Purdue University, West Lafayette, IN, USA.

[6]Applied Physics Graduate Program, Smalley-Curl Institute, Rice University, Houston, Texas, 77005, USA.

[7]Shared Equipment Authority, SIMS Laboratory, Rice University, Houston, TX 77005, US

[8]Department of Chemistry, University of Washington, Seattle 98195.

[9]Univ Rennes, ENSCR, CNRS, ISCR-UMR 6226, Rennes F-35000, France.

[10]Department of Chemistry, Rice University, Houston, Texas 77005, USA.

[11]X-Ray Science Division, Argonne National Laboratory, Argonne, IL, USA

[12] Univ Rennes, INSA Rennes, CNRS, Institut FOTON - UMR 6082, Rennes F-35000, France.

***Correspondence to: adm4@rice.edu, jacky.even@insa-rennes.fr**

Realizing solution-processed heterostructures is a long-enduring challenge in halide perovskites because of solvent incompatibilities that disrupt the underlying layer. By leveraging the solvent dielectric constant and Gutmann donor number, we could grow phase-pure two-dimensional (2D) halide perovskite bilayer stacks of the desired composition, thickness, and bandgap onto 3D perovskites without dissolving the underlying substrate. Characterization reveals a 3D-2D transition region of 20 nm, mainly determined by the roughness of the bottom 3D layer. Thickness dependence of the 2D perovskite layer reveals the anticipated trends for n-i-p and p-i-n architectures, consistent with band alignment and carrier transport limits for 2D perovskites. We measure a photovoltaic efficiency of 24.5%, with exceptional stability of T99>2000 hours, implying that the 3D/2D bilayer inherits the intrinsic durability of 2D perovskite without compromising efficiency.

https://www.science.org/doi/10.1126/science.abq7652; SCIENCE 377, ISSUE 6613, PP 1425-1430 (2022) DOI: 10.1126/SCIENCE.ABQ7652

One sentence summary: Design and fabrication of solution-processed scalable 3D|2D heterostructures for highly efficient and durable conversion of light to electrical energy.

Main

The progressive increase in the power conversion efficiency (PCE) of solution-processed perovskite solar cells (PSCs) (*1*, *2*) has been enabled in part by strategies to passivate the grain boundaries and interfaces between the perovskite absorber and the charge transport layers (*3*–*9*). Two-dimensional (2D) halide perovskites (HaP) passivation layers, which have been the most effective in improving the open-circuit voltage (V_{OC}) and fill factor (FF) (*10*–*13*), are commonly grown by spin-coating an organic cation dispersed in isopropyl alcohol or chloroform on top of 3D HaPs(*14*, *15*). This coating removes some excess lead iodide (PbI_2) from the 3D perovskite layer to then form heterogeneous 2D phases or ultrathin layers of wide bandgap 2D HaP (*16*–*18*).

These advances have enhanced durability, as demonstrated recently using damp-heat tests by Wolf *et al*., the lack of control over the phase purity, film thickness, orientation, and structural phase of the 2D HaP has limited their use as an interfacial passivation layer(*19*, *20*). A solvent-free growth of the 2D BA_2PbI_4 perovskite on the 3D film by controlling the pressure, temperature, and time was demonstrated by Noh *et al*., indicating the importance of a high-quality 3D/2D interface (*21*). However, such solid-state in-plane growth is difficult to scale to large areas. Thus, the fabrication of solution-processed heterostructures of 3D|2D HaP with the desired energy levels, thickness, and orientation has been lacking.

We now report a solvent design principle for fabricating solution-processed 3D/2D HaP bilayer structures with desired film thickness and phase purity of any 2D HaP, including Ruddlesden-Popper (RP), Dion-Jacobson (DJ), or alternating cation interlayer (ACI), described by the general formula of $L'A_{n-1}B_nX_{3n+1}$ where L': long-chain organic

cation, A: small monovalent cation B: divalent metal, and X: monovalent anion, and n: number of PbI_6 bonded octahedra along the stacking axis. Our approach leverages two essential properties of the processing solvents, the dielectric constant (ε_r) and the Gutmann donor number (D_N), which controls the coordination between the precursor ions and the solvent (*22*). Processing solvents with dielectric constant ε_r>30 and Gutmann number, 5<D_N<18 could effectively dissolve the 2D HaP powders without dissolving or degrading the underlying 3D perovskite film during processing using spin coating, doctor blading, or slot die coating.

Control over the different n-value and film thicknesses allowed us to progressively tune the heterostructure from a type I to a type II with the 2D perovskites acting as a transport layer. We achieved a PCE of 24.5% with a high open-circuit voltage (V_{OC}) of 1.2 V in a regular n-i-p device using a RP 2D $BA_2MA_2Pb_3I_{10}$ perovskite with a thickness of 50 nm. Importantly, a comparison of the International Summit on Organic Photostability ISOS-L-1 protocol [Maximum Power Point tracking under ambient conditions] stability of 3D/phase-pure (PP) 2D HaP bilayer PSC with the 2D passivated 3D, control-3D, and control-2D PSCs showed that the 3D/PP-2D HaP bilayer device exhibited exceptional stability with T_{99}>2000 hours. Thus, these structures had the durability of the 2D perovskite films without compromising PCE (*23*).

The comprehensive selection criteria for solvents that could selectively dissolve either the 2D (or 3D) HaP without disrupting the underlying 3D (or 2D) layer was based on the dielectric constant and the Gutmann donor number (Fig. 1A). These two distinct dissolve any ionic compound by screening the Coulomb attraction between the ions, whereas the Gutmann donor number describes the Lewis basicity of the solvent and measures the extent to which coordination compounds may form between solvent and

https://www.science.org/doi/10.1126/science.abq7652; SCIENCE 377, ISSUE 6613, PP 1425-1430 (2022) DOI: 10.1126/SCIENCE.ABQ7652

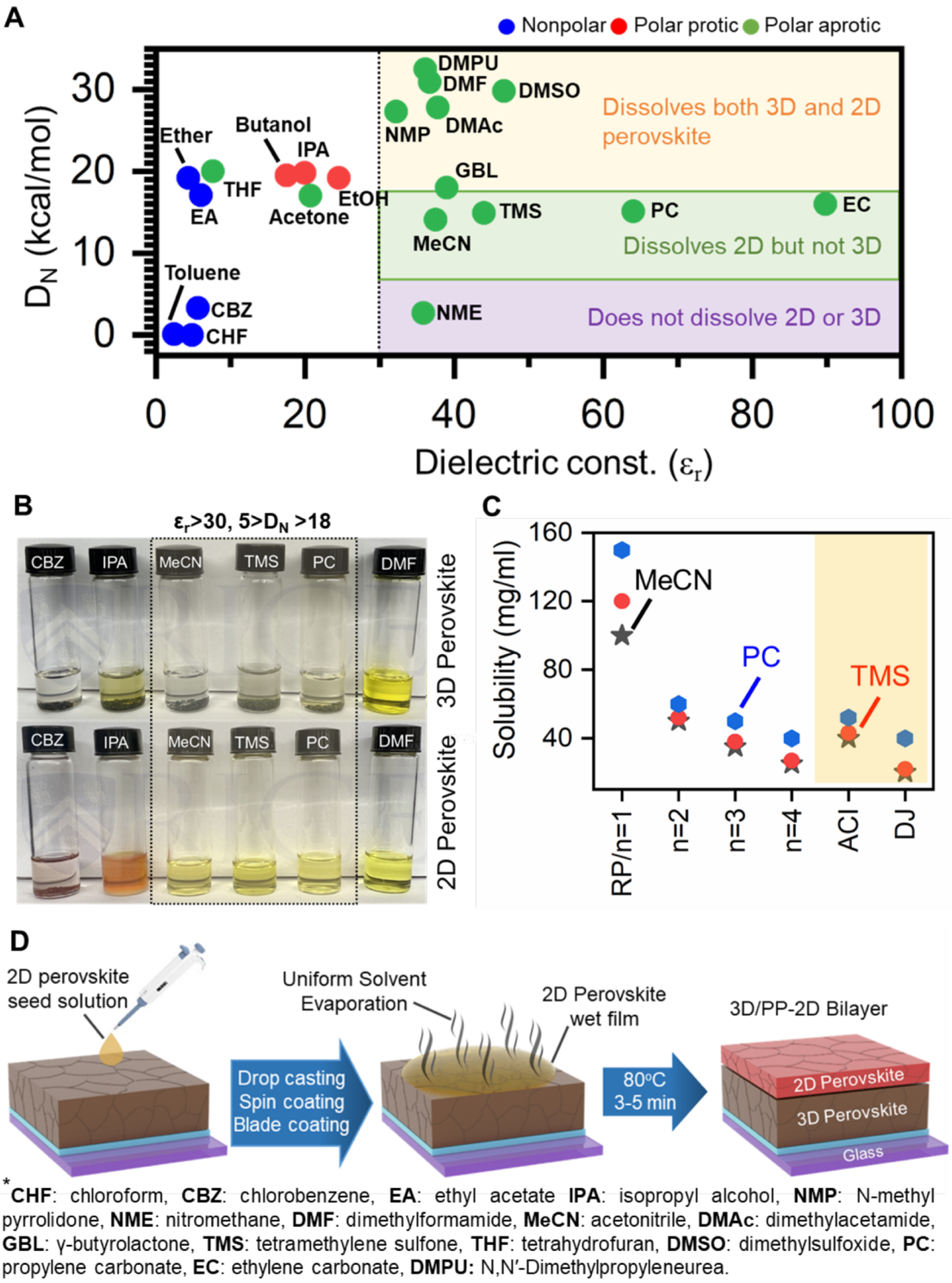

*CHF: chloroform, CBZ: chlorobenzene, EA: ethyl acetate IPA: isopropyl alcohol, NMP: N-methyl pyrrolidone, NME: nitromethane, DMF: dimethylformamide, MeCN: acetonitrile, DMAc: dimethylacetamide, GBL: γ-butyrolactone, TMS: tetramethylene sulfone, THF: tetrahydrofuran, DMSO: dimethylsulfoxide, PC: propylene carbonate, EC: ethylene carbonate, DMPU: N,N′-Dimethylpropyleneurea.

Figure 1. Design principle for fabricating a solution-processed 3D/phase-pure 2D HaP bilayer stack. (A) Plot showing different solvents based on the dielectric constant (ε_r), and the Gutmann number (D_N) to identify the differences in solubility of the 3D and 2D perovskite powders for making a 3D|2D bilayer stack. (B) Optical images of 2D (RP $BA_2MAPb_2I_7$) and 3D perovskite powders in different solvents. **C.** Solubility of RP $BA_2MA_{n-1}Pb_nI_{3n+1}$ (n=1-4), DJ, $(4AMP)MAPb_2I_7$, and AC $(GA)MA_2Pb_2I_7$-based 2D perovskites (where BA is butylamine, MA is methylammoniume, AMP is aminomethyl piperidine and GA is guanidinium) in the solvents MeCN, TMS, and PC as shown. **(D)** Fabrication steps of a 3D/2D HaP bilayer stack.

cations (high donor number) or between the precursors themselves (low donor number) in the absence of competitive binding of the solvent (*24*, *25*). For example, in the precursor solution comprised of methylammonium iodide (MAI), formamidinium iodide (FAI), and PbI_2, a solvent with a high Gutmann number would strongly coordinate with divalent metal centers (Pb^{2+}) and suppress the formation of molecular iodoplumbates complexes for example, $[PbI_{6-x}(solvent)_x]^{-(4-x)}$, where $x \leq 6$ or molecular clusters that would otherwise form in a solvent with low Gutmann number. The strength of these interactions determined the differences in the solubility of the 3D and 2D HaP powders in various solvents (Fig. 1A).

Typical vials of RP 2D ($BA_2MAPb_2I_7$) and the 3D HaP powders (Fig. 1B) illustrate their solubility in different solvents. Polar aprotic solvents (green dots) with a dielectric constant > 30, such as *N*, *N*-dimethylformamide (DMF), and dimethyl sulfoxide (DMSO), fully dissolved both 3D and 2D HaP. Solvents such as acetonitrile (MeCN), tetramethyl sulfone (TMS), propylene carbonate (PC), and ethylene carbonate (EC) also have a dielectric constant > 30 but did not dissolve the 3D HaP powders because their weak Lewis basicity (D_N value less than 18 kcal/mol) made the formation of Pb^{2+} solvent coordination complexes unlikely. However, these solvents completely dissolved the 2D perovskite powders. This difference is consistent with 3D perovskite lattices being more stable and difficult to disrupt with solvents of intermediate D_N than the 2D perovskites and implied the presence of additional favorable interactions of these solvents with the organic spacer cations (readily accessible from the edges of the slabs) that were absent in the 3D perovskites.

We observed that both nonpolar (blue dots) and polar protic solvents (red dots) did not completely dissolve the 2D HaP powders (Fig. 1B). As controls, we also tested

solvents with a high Gutmann number and low dielectric constant, such as tetrahydrofuran (D_N=20 kcal/mol, ε_r=7.6), and vice versa, such as nitromethane (NME) (D_N=2.7 kcal/mol, ε_r=35.9), both of which did not dissolve the 2D perovskite powders (see Fig. S1 and S2). Taken together, these results implied that solvents with a dielectric constant > 30 and the Gutmann number $5<D_N<18$ kcal/mol should enable the fabrication of 3D|2D HaP bilayers without disrupting or degrading the underlying 3D HaP film.

To fabricate 3D|2D HaP bilayers with different phases of 2D perovskite and having desired n-values, and thicknesses, we tested the solubility of the archetypical RP 2D perovskites ($BA_2MA_{n-1}Pb_nI_{3n+1}$ with n=1-4) and other crystal phases such as DJ ($(4AMP)MAPb_2I_7$), and ACI ($(GA)MA_2Pb_2I_7$) in the identified 2D perovskite-selective solvents (Fig. 1C). Because of its high polarity, propylene carbonate dissolved the 2D RP phases better than tetramethyl sulfone or acetonitrile. In general, we observed an overall decrease in the solubility of RP 2D HaPs with increasing *n* value, from greater than 100 mg/ml for *n*=1 to 30 to 40 mg/ml for *n*=4. The decrease in the solubility as a function of increasing n-value was consistent with the increase in inorganic lattice fraction of the 2D HaP as the n-value approached 3D composition.

In addition, the *n*=2 ACI, and DJ perovskites exhibited low solubilities of 20 to 40 mg/ml and 10 to 25 mg/ml, respectively, which was consistent with the structure of ACI and DJ 2D perovskites, which was near that of 3D with short interlayer cations that reflected the role of organic spacer cations in the dissolution process. Of all the target solvents, the high volatility of MeCN [boiling point (b.p.) ≈ 82°C] compared to the others, such as TMS (b. p.≈ 285°C), PC (b. p.≈ 242°C), and EC (b. p.≈ 248°C), made it attractive for low-temperature processing without affecting the stability of the entire stack (see Fig. S3, S4, and Movie S1, S2). We focused on the solvent MeCN for fabricating the targeted 3D|2D HaP bilayer.

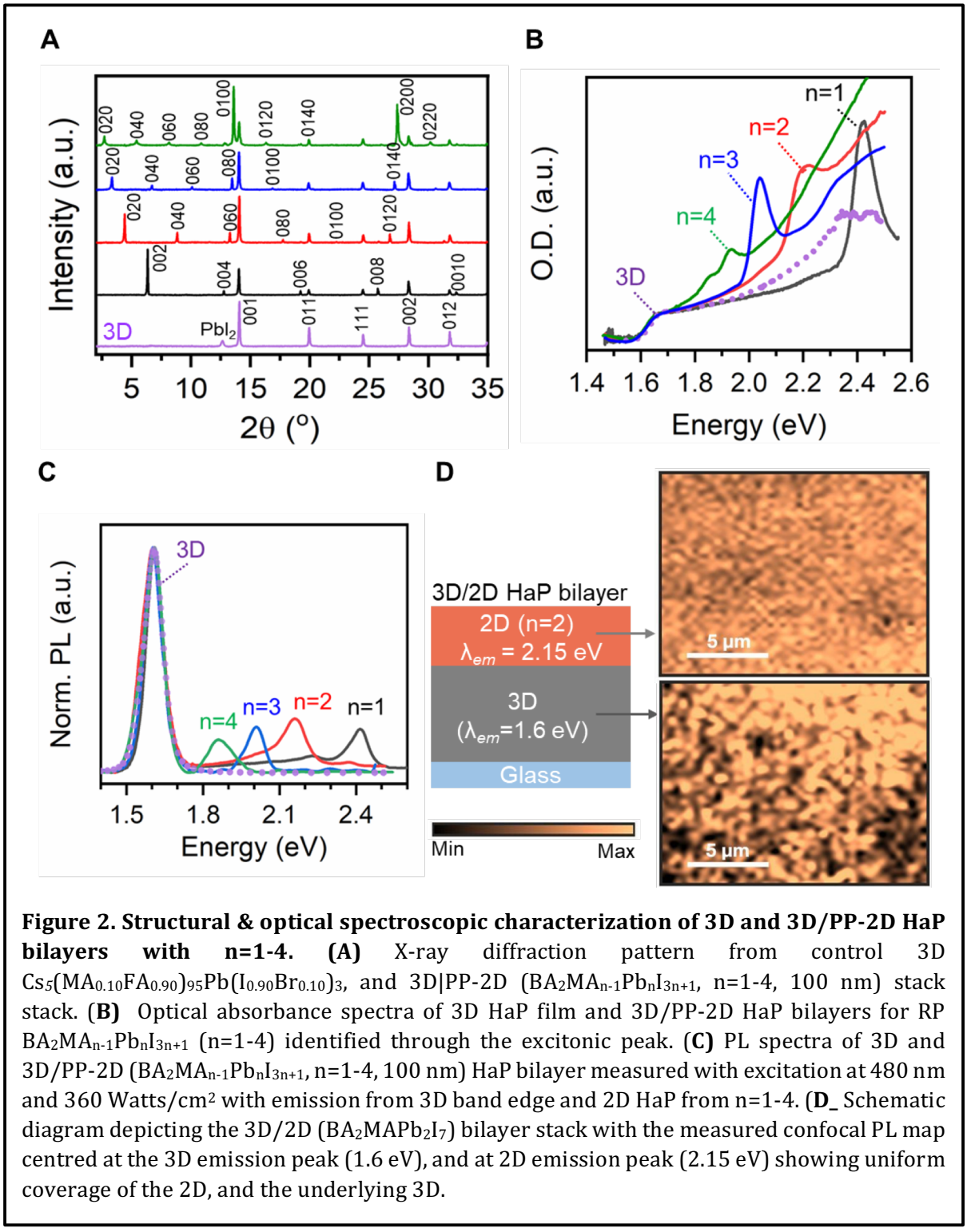

Figure 2. Structural & optical spectroscopic characterization of 3D and 3D/PP-2D HaP bilayers with n=1-4. (A) X-ray diffraction pattern from control 3D $Cs_5(MA_{0.10}FA_{0.90})_{95}Pb(I_{0.90}Br_{0.10})_3$, and 3D|PP-2D ($BA_2MA_{n-1}Pb_nI_{3n+1}$, n=1-4, 100 nm) stack stack. **(B)** Optical absorbance spectra of 3D HaP film and 3D/PP-2D HaP bilayers for RP $BA_2MA_{n-1}Pb_nI_{3n+1}$ (n=1-4) identified through the excitonic peak. **(C)** PL spectra of 3D and 3D/PP-2D ($BA_2MA_{n-1}Pb_nI_{3n+1}$, n=1-4, 100 nm) HaP bilayer measured with excitation at 480 nm and 360 Watts/cm^2 with emission from 3D band edge and 2D HaP from n=1-4. **(D_** Schematic diagram depicting the 3D/2D ($BA_2MAPb_2I_7$) bilayer stack with the measured confocal PL map centred at the 3D emission peak (1.6 eV), and at 2D emission peak (2.15 eV) showing uniform coverage of the 2D, and the underlying 3D.

The protocols for fabricating the 3D|2D HaP bilayer using spin coating, drop-casting, blade coating, or slot-die coating (Fig. 1D) followed our recent work on obtaining phase-pure 2D HaP films. We created a stable dispersion of 2D perovskite seed solution by dissolving the parent crystal powders in MeCN (see Fig. S5 and detailed discussion in

the SI)(*26*, *27*). In general, other than the solvents with Gutmann number $5<D_N<18$ kcal/mol, any Pb^{2+}-weakly coordinating solvents like DMF, GBL, and DMAc, compared to DMSO can produce a dispersion of 2D perovskite seed solution. The precursor solution with 2D perovskite seeds was coated on top of a 3D HaP layer ($Cs_5(MA_{0.10}FA_{0.90})_{95}Pb(I_{0.90}Br_{0.10})_3$), and then annealed at 80°C for 5 min. We also used other scalable techniques, such as doctor blading, drop-casting, and blade-coating coating (see Fig. S6) to demonstrate the industrial viability of the process. By controlling the concentration and deposition technique, we tuned the thickness of the 2D perovskite layer on top of the 3D film ranging from sub-10 nm to sub-micrometer scales (see Fig. S7).

Using the design approach described in Fig. 1, we fabricated a 3D|2D HaP (RP $BA_2MA_{n-1}Pb_nI_{3n+1}$, (n=1-4)) bilayer stack and characterized its phase purity using x-ray diffraction (XRD), optical absorbance, and photoluminescence (PL) techniques. For the XRD pattern for the control-3D and 3D|2D HaP bilayers with different 2D RP $BA_2MA_{n-1}Pb_nI_{3n+1}$ perovskite (n=1-4 Fig. 2A), matching the low angle Bragg peaks with the corresponding simulated patterns suggested that the overlying 2D HaP layer had high phase purity (see Fig. S8). The phase purity was further confirmed with absorbance (Fig. 2B) and PL (Fig. 2C) measurements. The optical absorbance revealed the presence of a 3D HaP band-edge at 1.6 eV for the control film which was accompanied by a sharp excitonic peak varying from 2.4 eV (n=1) to 1.9 eV (n=4) corresponding to the different n-values in the 3D/2D bilayer. The steady-state PL measurements further confirmed the phase purity of the 3D/2D HaP bilayers. We did not observe any change in the bandgap of the underlying 3D HaP, indicating that the presence of the 2D HaP layer did not disrupt the 3D perovskite.

To further assess the spatial homogeneity of the 3D/2D HaP bilayer, we monitored the PL emission centered at the 3D peak (1.6 eV) and the 2D (n=2, 2.15 eV) peak using

confocal microscopy (see Fig. 2D). We observed a uniform emission over a large area of 20 μm by 20 μm from the 2D, as well as the underlying 3D HaP layer, confirming the homogeneity of the 3D/2D HaP bilayer stack. These measurements indicated we had grown highly crystalline phase pure-2D (PP-2D) HaP of varying *n*-values on the 3D surface. This fabrication process also worked well with the pure $FAPbI_3$ and $MAPbI_3$ 3D HaP, demonstrating its broad applicability (see Fig. S9).

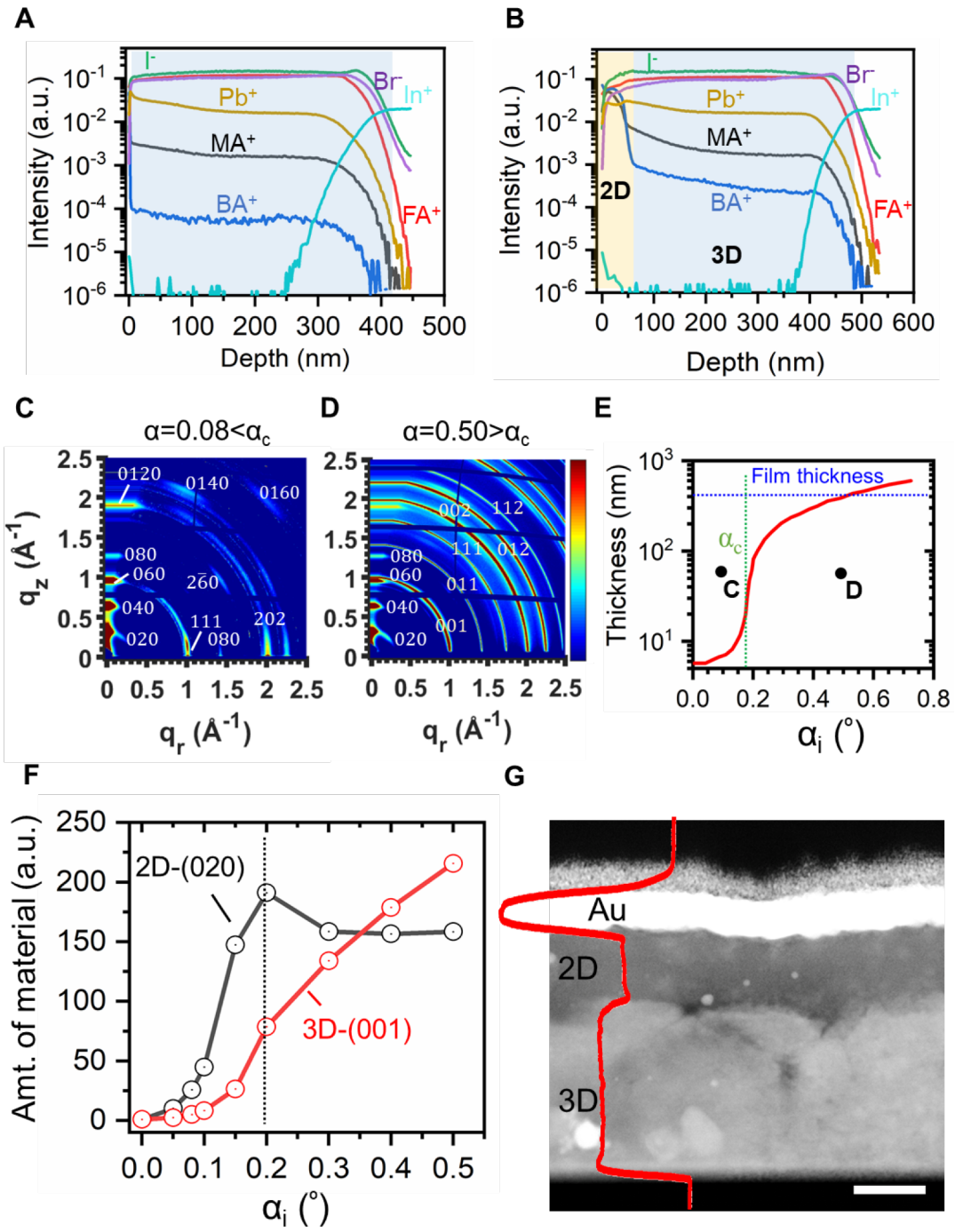

Figure 3. 3D/PP-2D HaP interface characterization. (A) ToF-SIMS depth profile of the control $Cs_5(MA_{0.10}FA_{0.90})_{95}Pb(I_{0.90}Br_{0.10})_3$ 3D perovskite film and **(B)** 3D|PP-2D ($BA_2MAPb_2I_7$) HaP stack deposited on top of indium tin oxide shows the distribution of different ions across the thickness and the sharpness of the heterointerface. (**C** and **D)** Angle-dependent GIWAXS pattern of the 3D|PP-2D (RP $BA_2MAPb_2I_7$) HaP stack show evolution of 2D and 3D perovskites for increasing incident angle. The most efficient 3D/PP-2D HaP solar cell was obtained for $BA_2MA_2Pb_3I_{10}$ RP perovskite, which exhibited mixed vertical orientation shown in Fig. 4. **(E)** Simulated x-ray penetration depth curve for the RP-2D HaP at various incident angles showing the critical angle and the thickness of the probed film. (**F)** Amount of 2D and 3D HaP materials extracted from the angular integrated diffraction peaks. (**G)** Cross-sectional dark-field HR-TEM image of the 3D/PP-2D ($BA_2MAPb_2I_7$) HaP stack with the overlaying intensity profile (in red color) shows transition width from 3D to 2D of 20 nm. The scale bar is 100 nm.

We used several techniques to characterize the interface between the 3D and PP-2D layers. The time-of-flight secondary ion mass spectroscopy (ToF-SIMS) depth profile of the control 3D (Fig. 3A) and 3D/PP-2D HaP bilayer (Fig. 3B) revealed the distribution of ions as a function of film thickness. Upon introduction of $BA_2MAPb_2I_7$ 2D perovskite layer on top of the 3D film, in addition to the Cs_2I^+, Cs_2Br^+ halide ions, and $CH_5N_2^+$ (FA^+) organic cations, we observed higher intensity of the $C_4H_{12}N^+$ (BA^+) compared to the background BA^+ intensity (see detailed discussion in SI) and CH_6N^+ (MA^+) ions. These ions were uniformly distributed for a thickness of 50 nm, after which there was a sharp decrease in the concentration. Fitting the change in intensity of the BA^+ to the background (representing no BA) yielded an interface transition of 20 nm from the top 2D layer to the underlying 3D HaP. The TOF-SIMS measurements of the 3D|PP-2D (RP $BA_2MA_2Pb_3I_{10}$) bilayer stack show similar results (see Fig. S10).

The grazing incidence wide-angle scattering (GIWAXS) spectra of the 3D|PP-2D HaP bilayer for different incident angles (or depth) (Fig. 3C, and 3D) shows the presence of horizontal oriented $BA_2MAPb_2I_7$ 2D HaP on the surface ($\alpha = 0.08°$), and the 3D HaP ($Cs_5(MA_{0.10}FA_{0.90})_{95}Pb(I_{0.90}Br_{0.10})_3$) in the form of rings at the bottom ($\alpha = 0.5°$) (also see Fig. S11, detailed discussion in SI). This result is well correlated with the calculated x-ray penetration depth curve for the RP-2D HaP, showing a critical angle (α_c) of 0.181° (Fig. 3E)(*28*, *29*). The integrated area under the (020) peak (2D signature feature) and the (111)/(001) peak (3D signature feature) from the GIWAXS spectra for various incident angles (0 to 0.5°) (Fig. 3F) revealed the 3D|PP-2D interface at an incident angle of 0.2°. The integrated area under the (020) peak became invariant, whereas the (111)/ (001) increased, which confirmed the presence of a 2D HaP layer with a thickness of 50 to 60 nm stacked on top of the 3D HaP film as estimated from the penetration depth curve. On the other hand, the $BA_2MA_2Pb_3I_{10}$ 2D HaP shows a mixed orientation in the 3D|PP-2D

(n=3, RP) HaP bilayer stack with similar interfacial characteristics (see detailed GIWAXS analysis in Fig. S12). The presence of some texture in the orientation as in the n=3, RP perovskite is required for efficient charge transfer through the 2D perovskite resulting in the efficient 3D|PP-2D bilayer HaP solar cells as will be shown in Fig. 4 (*26*, *27*). The dark-field cross-sectional high-resolution transmission electron microscopy (HRTEM) image of the 3D|PP-2D (RP $BA_2MAPb_2I_7$) HaP bilayer grown on the silicon substrate (with gold and carbon as the top protective layer, Fig. 3G) verified the homogeneity of the 2D HaP layer on top of the 3D HaP thin film. The average intensity profile (indicated in red) showed an interfacial 3D|PP-2D sharpness of 20 nm, which was consistent with the TOF-SIMS measurements and matched the roughness of the control-3D film (see Fig. S13). The HRTEM image of the 3D|PP-2D (RP $BA_2MA_2Pb_3I_{10}$) HaP bilayer stack also showed similar interfacial characteristics (see Fig. S14). All of these results demonstrated that our solvent design strategy allowed for the fabrication of 3D/PP- 2D bilayers with a high-quality interface without destroying or altering the crystallinity of the underlying 3D perovskite.

We fabricated solar cells with the 3D|PP-2D HaP bilayer perovskites and measured their performance and durability. We first created an energy level diagram for the 2D HaP, RP $BA_2MA_{n-1}Pb_nI_{3n+1}$ (n=1-4), with the 3D perovskite $Cs_5(MA_{0.10}FA_{0.90})_{95}Pb(I_{0.90}Br_{0.10})_3$ (Fig. 4A) based on values predicted from first-principles calculations (see Fig. S15) and corroborated with photoemission yield spectroscopy (PES) and absorption measurements(*30*) (see Fig. S16 to S18). We observed a type II band alignment between the 3D and the *n*=3 2D HaP with a near-perfect alignment of valence band edges for 3D and 2D HaP, which is ideal for extracting holes but presents a large energy barrier for electrons (Fig. S19). The 3D|PP-2D (n=1, n=2) HaP bilayer stack shows a Type I alignment, further confirmed by fabricating solar cells showing a barrier for charge extraction using

higher thicknesses of the corresponding 2D layers (see detailed discussion in the SI, and Fig. S20). As a result, we fabricated n-i-p PSCs with the architecture FTO|SnO_2|3D|PP-2D(n=3)/spiro-OMeTAD|Au, controlling the PP-2D (n=3) HaP thickness by spin coating different concentration of 2D perovskite solution in MeCN (see Fig. S21).

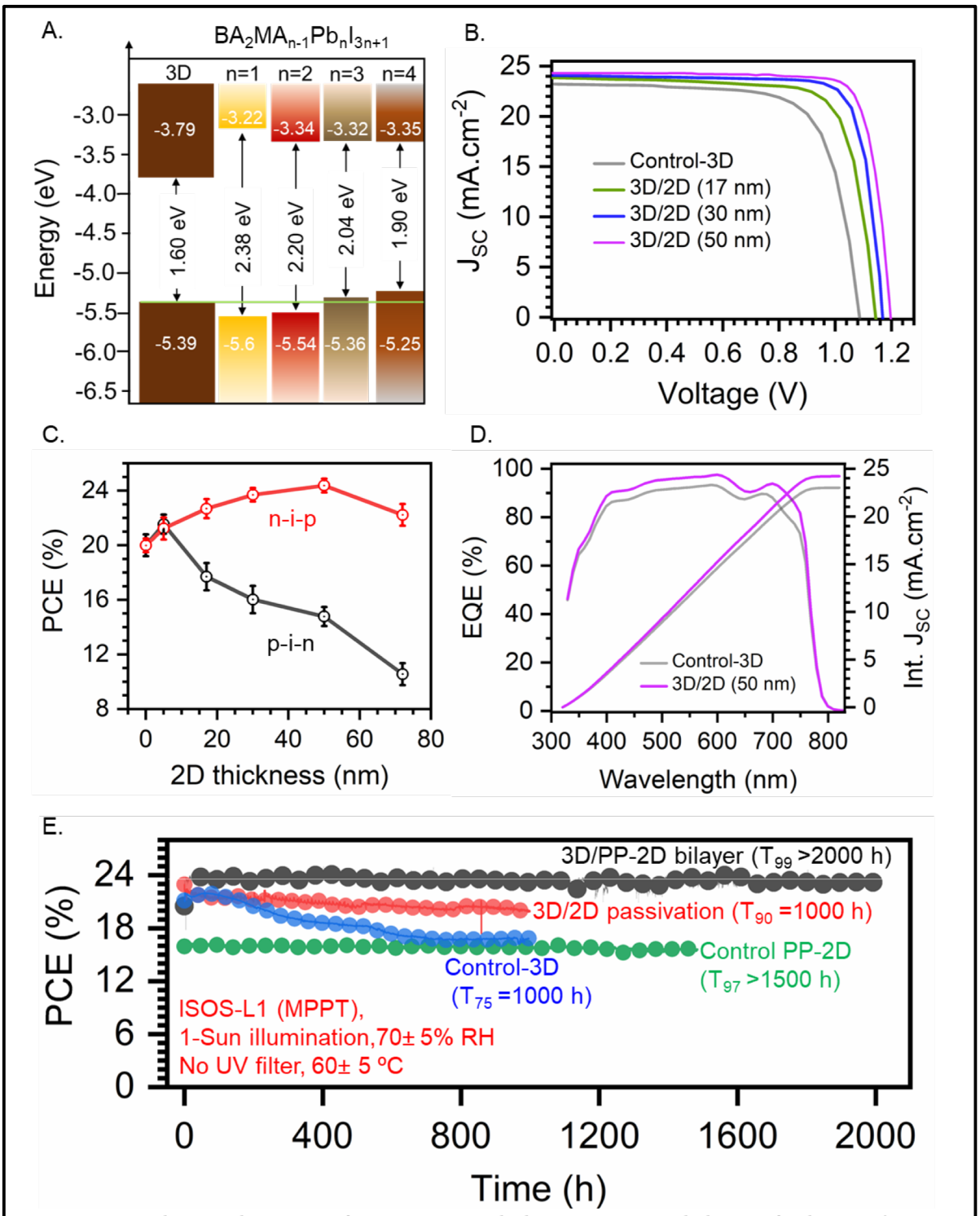

Figure 4. Photovoltaic performance and long-term stability of the 3D|PP-2D ($BA_2MA_2Pb_3I_{10}$) HaP bilayer solar cells. (A) Energy-level alignment for different n-values (n≤4) of 2D perovskite with the 3D perovskite layer with an error of ±0.05eV. **(B)** Current-voltage curves of the champion 3D/PP-2D n-i-p PSCs as a function of the 2D layer thickness obtained by spin coating different concentration of the 2D perovskite solution in MeCN. **(C)** Variation in PCE of the n-i-p and p-i-n planar 3D|PP-2D PSCs as a function of 2D perovskite layer thickness. **(D)** External quantum efficiency of the device with and without the 2D layer, showing the absorption and current generation ability of the stack. **(E)** ISOS-L-1 stability measured at maximum power point tracking in ambient condition under continuous 1-sun illumination (55°C) for an epoxy encapsulated PSC. The initial PCE of the control device is 21%, the 3D|2D passivated device, 22.93%, the 3D|PP-2D bilayer PSC, 23.75% and the PP-2D perovskite device is 16.3%.

Figure 4B shows the current-voltage (J-V) characteristics for three selected thicknesses of 2D HaP layers with 3D HaP as the control. For n-i-p cells, increased 2D HaP thickness from 0 to 50 nm increased V_{OC} from 1.09 V to 1.2 V. This increase in the V_{OC} was accompanied by a slight increase in the FF from 0.80 to 0.84, and even a small increase in J_{SC} from 23.54 to 24.34 mA.cm^{-2} resulting in a peak PCE of 24.5% for a 2D HaP thickness of 50 nm with no hysteresis (Fig. S22 and S23). The PCE as a function of 2D HaP thickness shows that increasing the 2D HaP thickness beyond 50 nm decreased the overall PCE (Fig. 4C). We attributed this decrease in PCE to the reduced transport of the free charge carriers from 3D to the 2D HaP limited by the <100 nm diffusion length for a polycrystalline 2D n=3, RP HaP film with mixed oriented (*31*, *32*) (see PV statistics in Fig. S23).However, the p-i-n devices with ITO|PTAA|3D|PP-2D(*n*=3)|C60|BCP|Cu exhibited an increase in PCE for a 2D HaP thickness of 5 nm, consistent with recent studies of 2D|3D interfaces with an ultrathin 2D layer passivation followed by a drastic decrease for higher thicknesses of 2D HaP (Fig. 4C, black curve, and Fig. S24, S25)(*33*, *34*). The reduction in PCE was consistent with the energy band diagram (Fig. 4A and Fig. S19B), which showed a large barrier to electron collection in the p-i-n geometry.

To understand the increase in PV parameters (J_{SC}, V_{OC}, and FF) of the 3D|PP-2D HaP bilayer solar cells, we performed optical and self-consistent transport modelling to simulate the PV characteristics which are supported by the surface photovoltage (SPV), steady-state photoluminescence (PL), and time-resolved PL measurements. The optical modelling revealed that the 2D HaP layer increased the photogeneration of the bilayer stack and improved J_{SC} (see Fig. S26). This result was consistent with the observed increase in the J_{SC} by 1.5 mA/cm^2 as we went from the 3D control to the champion 3D|PP-2D HaP bilayer device validated by external quantum efficiency (EQE) measurements shown in

Fig. 4D and the change in EQE (ΔEQE) between them (see Fig. S27, S28 and detailed discussion in SI).

The self-consistent transport simulation predicted reduced recombination at the 3D/HTL interface after the introduction of a 2D HaP layer, thereby improving the V_{OC} and FF (see Fig. S29). To corroborate these results, we measured the surface photovoltage (SPV) using scanning Kelvin probe microscopy (SKPM) on the ITO|SnO_2|3D|PP-2D (RP $BA_2MA_2Pb_3I_{10}$) stack, which showed an increase in the SPV as a function of the 2D layer thickness (see Figure S30, S31). This result suggested an increase in the quasi-Fermi level separation related to the V_{OC} of the device(*35*–*38*). The dark I-V curve traces of the solar cells further confirm the increase in V_{OC} (see detailed discussion in SI, and Fig. S32). Additionally, the steady-state PL and time-resolved photoluminescence (TRPL) measurements on the ITO|SnO_2|3D|PP-2D (RP $BA_2MA_2Pb_3I_{10}$) stack showed enhanced PL emission and increased charge carrier lifetime up to a 2D HaP thickness of 50 (see Figure S33) but decreases for the higher thickness of 2D HaPs. The overlaying 2D HaP minimized the nonradiative recombination pathways between the 3D perovskite/electrode (HTL) interface as confirmed by the transport modeling measurements, improving both the FF and the V_{OC} of the 3D/PP-2D devices(*15*, *39*).

We tested the long-term operational stability of our 3D|PP-2D bilayer encapsulated device following the ISOS-L-1 protocol (*23*) (see Fig. 4G). After 2000 hours of continuous illumination, the 3D|PP-2D HaP bilayer device showed negligible degradation with T_{99}>2000 hours, whereas the control 3D device lost 25% of its initial PCE. As controls, we also measured the stability of the 3D PSC passivated with a spin-coated organic cation, butylammonium iodide, and compared it with our 3D|PP-2D PSCs using the same conditions. The 2D HaP passivated 3D PSCs show a 10% loss of efficiency

after 1000 hours of continuous operation, consistent with other recent reports(*4*, *19*). We also measured a pure 2D HaP control device, which showed a T_{97}> 1500 hours, implying that the 3D/PP-2D bilayer perovskite has acquired the inherent stability of the 2D perovskite material.

REFERENCES

1. J. Jeong, M. Kim, J. Seo, H. Lu, P. Ahlawat, A. Mishra, Y. Yang, M. A. Hope, F. T. Eickemeyer, M. Kim, Pseudo-halide anion engineering for α-FAPbI3 perovskite solar cells. *Nature*. **592**, 381–385 (2021).

2. H. Min, D. Y. Lee, J. Kim, G. Kim, K. S. Lee, J. Kim, M. J. Paik, Y. K. Kim, K. S. Kim, M. G. Kim, Perovskite solar cells with atomically coherent interlayers on SnO2 electrodes. *Nature*. **598**, 444–450 (2021).

3. Q. Jiang, Y. Zhao, X. Zhang, X. Yang, Y. Chen, Z. Chu, Q. Ye, X. Li, Z. Yin, J. You, Surface passivation of perovskite film for efficient solar cells. *Nature Photonics*. **13**, 460–466 (2019).

4. F. Zhang, S. Y. Park, C. Yao, H. Lu, S. P. Dunfield, C. Xiao, S. Uličná, X. Zhao, L. Du Hill, X. Chen, Metastable Dion-Jacobson 2D structure enables efficient and stable perovskite solar cells. *Science*. **375**, 71–76 (2022).

5. X. Zheng, Y. Hou, C. Bao, J. Yin, F. Yuan, Z. Huang, K. Song, J. Liu, J. Troughton, N. Gasparini, Managing grains and interfaces via ligand anchoring enables 22.3%-efficiency inverted perovskite solar cells. *Nature Energy*. **5**, 131–140 (2020).

6. Y. Liu, S. Akin, L. Pan, R. Uchida, N. Arora, J. V. Milić, A. Hinderhofer, F. Schreiber, A. R. Uhl, S. M. Zakeeruddin, Ultrahydrophobic 3D/2D fluoroarene bilayer-based water-resistant perovskite solar cells with efficiencies exceeding 22%. *Science advances*. **5**, eaaw2543 (2019).

7. N. K. Noel, A. Abate, S. D. Stranks, E. S. Parrott, V. M. Burlakov, A. Goriely, H. J. Snaith, Enhanced photoluminescence and solar cell performance via Lewis base passivation of organic–inorganic lead halide perovskites. *ACS nano*. **8**, 9815–9821 (2014).

8. D. W. DeQuilettes, S. Koch, S. Burke, R. K. Paranji, A. J. Shropshire, M. E. Ziffer, D. S. Ginger, Photoluminescence lifetimes exceeding 8 μs and quantum yields exceeding 30% in hybrid perovskite thin films by ligand passivation. *ACS Energy Letters*. **1**, 438–444 (2016).

9. I. L. Braly, D. W. DeQuilettes, L. M. Pazos-Outón, S. Burke, M. E. Ziffer, D. S. Ginger, H. W. Hillhouse, Hybrid perovskite films approaching the radiative limit with over 90% photoluminescence quantum efficiency. *Nature Photonics*. **12**, 355–361 (2018).

10. A. A. Sutanto, P. Caprioglio, N. Drigo, Y. J. Hofstetter, I. Garcia-Benito, V. I. Queloz, D. Neher, M. K. Nazeeruddin, M. Stolterfoht, Y. Vaynzof, 2D/3D perovskite engineering eliminates interfacial recombination losses in hybrid perovskite solar cells. *Chem*. **7**, 1903–1916 (2021).

11. G. Wu, R. Liang, M. Ge, G. Sun, Y. Zhang, G. Xing, Surface Passivation Using 2D Perovskites toward Efficient and Stable Perovskite Solar Cells. *Advanced Materials*. **34**, 2105635 (2022).

12. G. Li, J. Song, J. Wu, Z. Song, X. Wang, W. Sun, L. Fan, J. Lin, M. Huang, Z. Lan, Efficient and Stable 2D@ 3D/2D Perovskite Solar Cells Based on Dual Optimization of Grain Boundary and Interface. *ACS Energy Letters*. **6**, 3614–3623 (2021).

13. M. A. Mahmud, T. Duong, J. Peng, Y. Wu, H. Shen, D. Walter, H. T. Nguyen, N. Mozaffari, G. D. Tabi, K. R. Catchpole, Origin of efficiency and stability enhancement in high-performing mixed dimensional 2D-3D perovskite solar cells: a review. *Advanced Functional Materials*. **32**, 2009164 (2022).

14. E. Jokar, P.-Y. Cheng, C.-Y. Lin, S. Narra, S. Shahbazi, E. Wei-Guang Diau, Enhanced performance and stability of 3D/2D tin perovskite solar cells fabricated with a sequential solution deposition. *ACS Energy Letters*. **6**, 485–492 (2021).

15. J. J. Yoo, S. Wieghold, M. C. Sponseller, M. R. Chua, S. N. Bertram, N. T. P. Hartono, J. S. Tresback, E. C. Hansen, J.-P. Correa-Baena, V. Bulović, An interface stabilized perovskite solar cell with high stabilized efficiency and low voltage loss. *Energy & Environmental Science*. **12**, 2192–2199 (2019).

16. T. Zhang, M. Long, M. Qin, X. Lu, S. Chen, F. Xie, L. Gong, J. Chen, M. Chu, Q. Miao, Stable and efficient 3D-2D perovskite-perovskite planar heterojunction solar cell without organic hole transport layer. *Joule*. **2**, 2706–2721 (2018).

17. P. Li, Y. Zhang, C. Liang, G. Xing, X. Liu, F. Li, X. Liu, X. Hu, G. Shao, Y. Song, Phase pure 2D perovskite for high-performance 2D–3D heterostructured perovskite solar cells. *Advanced materials*. **30**, 1805323 (2018).

18. F. Wang, X. Jiang, H. Chen, Y. Shang, H. Liu, J. Wei, W. Zhou, H. He, W. Liu, Z. Ning, 2D-quasi-2D-3D hierarchy structure for tin perovskite solar cells with enhanced efficiency and stability. *Joule*. **2**, 2732–2743 (2018).

19. R. Azmi, E. Ugur, A. Seitkhan, F. Aljamaan, A. S. Subbiah, J. Liu, G. T. Harrison, M. I. Nugraha, M. K. Eswaran, M. Babics, Damp heat–stable perovskite solar cells with tailored-dimensionality 2D/3D heterojunctions. *Science*, eabm5784 (2022).

20. M. Xiong, W. Zou, K. Fan, C. Qin, S. Li, L. Fei, J. Jiang, H. Huang, L. Shen, F. Gao, Tailoring Phase Purity in the 2D/3D Perovskite Heterostructures Using Lattice Mismatch. *ACS Energy Letters*. **7**, 550–559 (2022).

21. Y.-W. Jang, S. Lee, K. M. Yeom, K. Jeong, K. Choi, M. Choi, J. H. Noh, Intact 2D/3D halide junction perovskite solar cells via solid-phase in-plane growth. *Nature Energy*. **6**, 63–71 (2021).

22. V. Gutmann, Solvent effects on the reactivities of organometallic compounds. *Coordination Chemistry Reviews*. **18**, 225–255 (1976).

23. M. V. Khenkin, E. A. Katz, A. Abate, G. Bardizza, J. J. Berry, C. Brabec, F. Brunetti, V. Bulović, Q. Burlingame, A. Di Carlo, Consensus statement for stability assessment and reporting for perovskite photovoltaics based on ISOS procedures. *Nature Energy*. **5**, 35–49 (2020).

24. J. C. Hamill Jr, J. Schwartz, Y.-L. Loo, Influence of solvent coordination on hybrid organic–inorganic perovskite formation. *ACS Energy Letters*. **3**, 92–97 (2017).

25. J. C. Hamill Jr, O. Romiluyi, S. A. Thomas, J. Cetola, J. Schwartz, M. F. Toney, P. Clancy, Y.-L. Loo, Sulfur-donor solvents strongly coordinate Pb2+ in hybrid organic–inorganic perovskite precursor solutions. *The Journal of Physical Chemistry C*. **124**, 14496–14502 (2020).

26. S. Sidhik, W. Li, M. H. Samani, H. Zhang, Y. Wang, J. Hoffman, A. K. Fehr, M. Wong, C. Katan, J. Even, Memory seeds enable high structural phase purity in 2D perovskite films for high-efficiency devices.

27. S. Sidhik, Y. Wang, W. Li, H. Zhang, X. Zhong, A. Agrawal, I. Hadar, I. Spanopoulos, A. Mishra, B. Traore, High-phase purity two-dimensional perovskites with 17.3% efficiency enabled by interface engineering of hole transport layer. *Cell Reports Physical Science*. **2**, 100601 (2021).

28. M. Tolan, M. Tolan, *X-ray scattering from soft-matter thin films: materials science and basic research* (Springer, 1999), vol. 148.

29. R. M. Kennard, C. J. Dahlman, J. Chung, B. L. Cotts, A. A. Mikhailovsky, L. Mao, R. A. DeCrescent, K. H. Stone, N. R. Venkatesan, Y. Mohtashami, Growth-Controlled Broad Emission in Phase-Pure Two-Dimensional Hybrid Perovskite Films. *Chemistry of Materials*. **33**, 7290–7300 (2021).

30. I. Spanopoulos, I. Hadar, W. Ke, Q. Tu, M. Chen, H. Tsai, Y. He, G. Shekhawat, V. P. Dravid, M. R. Wasielewski, Uniaxial expansion of the 2D Ruddlesden–Popper perovskite family for improved environmental stability. *Journal of the American Chemical Society*. **141**, 5518–5534 (2019).

31. M. Seitz, A. J. Magdaleno, N. Alcázar-Cano, M. Meléndez, T. J. Lubbers, S. W. Walraven, S. Pakdel, E. Prada, R. Delgado-Buscalioni, F. Prins, Exciton diffusion in two-dimensional metal-halide perovskites. *Nature communications*. **11**, 1–8 (2020).

32. E. D. Kinigstein, H. Tsai, W. Nie, J.-C. Blancon, K. G. Yager, K. Appavoo, J. Even, M. G. Kanatzidis, A. D. Mohite, M. Y. Sfeir, Edge States Drive Exciton Dissociation in Ruddlesden–Popper Lead Halide Perovskite Thin Films. *ACS Materials Letters*. **2**, 1360–1367 (2020).

33. M. Degani, Q. An, M. Albaladejo-Siguan, Y. J. Hofstetter, C. Cho, F. Paulus, G. Grancini, Y. Vaynzof, 23.7% Efficient inverted perovskite solar cells by dual interfacial modification. *Science advances*. **7**, eabj7930 (2021).

34. X. Wang, K. Rakstys, K. Jack, H. Jin, J. Lai, H. Li, C. S. K. Ranasinghe, J. Saghaei, G. Zhang, P. L. Burn, Engineering fluorinated-cation containing inverted perovskite solar cells with an efficiency of> 21% and improved stability towards humidity. *Nature communications*. **12**, 1–10 (2021).

35. S. Kavadiya, A. Onno, C. Boyd, Z. Yu, M. McGehee, Z. C. Holman, in *2020 47th IEEE Photovoltaic Specialists Conference (PVSC)* (IEEE, 2020), pp. 1439–1440.

36. I. Levine, A. Al-Ashouri, A. Musiienko, H. Hempel, A. Magomedov, A. Drevilkauskaite, V. Getautis, D. Menzel, K. Hinrichs, T. Unold, Charge transfer rates and electron trapping at buried interfaces of perovskite solar cells. *Joule*. **5**, 2915–2933 (2021).

37. L. Kronik, Y. Shapira, Surface photovoltage phenomena: theory, experiment, and applications. *Surface science reports*. **37**, 1–206 (1999).

38. R. Giridharagopal, J. T. Precht, S. Jariwala, L. Collins, S. Jesse, S. V. Kalinin, D. S. Ginger, Time-resolved electrical scanning probe microscopy of layered perovskites reveals spatial variations in photoinduced ionic and electronic carrier motion. *ACS nano*. **13**, 2812–2821 (2019).

39. J. Wang, W. Fu, S. Jariwala, I. Sinha, A. K.-Y. Jen, D. S. Ginger, Reducing surface recombination velocities at the electrical contacts will improve perovskite photovoltaics. *ACS Energy Letters*. **4**, 222–227 (2018).

40. Z. Jiang, X. Li, J. Strzalka, M. Sprung, T. Sun, A. R. Sandy, S. Narayanan, D. R. Lee, J. Wang, The dedicated high-resolution grazing-incidence X-ray scattering beamline 8-ID-E at the Advanced Photon Source. *Journal of synchrotron radiation*. **19**, 627–636 (2012).

41. Z. Jiang, GIXSGUI: a MATLAB toolbox for grazing-incidence X-ray scattering data visualization and reduction, and indexing of buried three-dimensional periodic nanostructured films. *Journal of Applied Crystallography*. **48**, 917–926 (2015).

42. A. L. Patterson, The Scherrer formula for X-ray particle size determination. *Physical review*. **56**, 978 (1939).

43. F. Sanchez-Bajo, F. L. Cumbrera, The use of the pseudo-Voigt function in the variance method of X-ray line-broadening analysis. *Journal of Applied Crystallography*. **30**, 427–430 (1997).

44. D.-M. Smilgies, Scherrer grain-size analysis adapted to grazing-incidence scattering with area detectors. *Journal of applied crystallography*. **42**, 1030–1034 (2009).

45. W. I. Goldburg, Dynamic light scattering. *American Journal of Physics*. **67**, 1152–1160 (1999).

46. B. J. Berne, R. Pecora, *Dynamic light scattering: with applications to chemistry, biology, and physics* (Courier Corporation, 2000).

47. W. Wien, Theorie der Warmestrahlung. *Physik*. **3**, 209 (1915).

48. W. Kohn, L. J. Sham, Self-consistent equations including exchange and correlation effects. *Physical review*. **140**, A1133 (1965).

49. J. M. Soler, E. Artacho, J. D. Gale, A. Garcia, J. Junquera, P. Ordejon, D. Sanchez-Portal, The SIESTA method for ab initio order-N materials simulation. *Journal of Physics: Condensed Matter*. **14**, 2745 (2002).

50. V. R. Cooper, Van der Waals density functional: An appropriate exchange functional. *Physical Review B*. **81**, 161104 (2010).

51. I. Hamada, M. Otani, Comparative van der Waals density-functional study of graphene on metal surfaces. *Physical Review B*. **82**, 153412 (2010).

52. S. F. Yuk, K. C. Pitike, S. M. Nakhmanson, M. Eisenbach, Y. W. Li, V. R. Cooper, Towards an accurate description of perovskite ferroelectrics: exchange and correlation effects. *Scientific reports*. **7**, 1–10 (2017).

53. N. Troullier, J. L. Martins, Efficient pseudopotentials for plane-wave calculations. *Physical review B*. **43**, 1993 (1991).

54. L. G. Ferreira, M. Marques, L. K. Teles, Approximation to density functional theory for the calculation of band gaps of semiconductors. *Physical Review B*. **78**, 125116 (2008).

55. L. Fernandez-Seivane, M. A. Oliveira, S. Sanvito, J. Ferrer, On-site approximation for spin–orbit coupling in linear combination of atomic orbitals density functional methods. *Journal of Physics: Condensed Matter*. **18**, 7999 (2006).

56. D. G. Billing, A. Lemmerer, Synthesis, characterization and phase transitions in the inorganic–organic layered perovskite-type hybrids [(CnH2n+ 1NH3) 2PbI4], n= 4, 5 and 6. *Acta Crystallographica Section B: Structural Science*. **63**, 735–747 (2007).

57. C. C. Stoumpos, D. H. Cao, D. J. Clark, J. Young, J. M. Rondinelli, J. I. Jang, J. T. Hupp, M. G. Kanatzidis, Ruddlesden–Popper hybrid lead iodide perovskite 2D homologous semiconductors. *Chemistry of Materials*. **28**, 2852–2867 (2016).

58. M. T. Weller, O. J. Weber, J. M. Frost, A. Walsh, Cubic perovskite structure of black formamidinium lead iodide, α-[HC (NH2) 2] PbI3, at 298 K. *The journal of physical chemistry letters*. **6**, 3209–3212 (2015).

59. E. Bitzek, P. Koskinen, F. Gahler, M. Moseler, P. Gumbsch, Structural relaxation made simple. *Physical review letters*. **97**, 170201 (2006).

60. B. Song, J. Hou, H. Wang, S. Sidhik, J. Miao, H. Gu, H. Zhang, S. Liu, Z. Fakhraai, J. Even, J. C Blancon, A. D. Mohite, D. Jariwala, Determination of Dielectric Functions and Exciton Oscillator Strength of Two-Dimensional Hybrid Perovskites. *ACS Materials Letters*. **3**, 148–159 (2021).

61. A. Tejada, S. Peters, A. Al-Ashouri, S. H. Turren-Cruz, A. Abate, S. Albrecht, F. Ruske, B. Rech, J. A. Guerra, L. Korte, Hybrid Perovskite Degradation from an Optical Perspective: A Spectroscopic Ellipsometry Study from the Deep Ultraviolet to the Middle Infrared. *Advanced Optical Materials*. **10**, 2101553 (2022).

62. M. Filipič, P. Loper, B. Niesen, S. De Wolf, J. Krč, C. Ballif, M. Topič, CH_3NH_3PbI_3 perovskite silicon tandem solar cells: characterization based optical simulations. *Optics Express*. **23**, A263 (2015).

63. J. Gong, X. Wang, X. Fan, R. Dai, Z. Wang, Z. Zhang, Z. Ding, Temperature dependent optica properties of SnO 2 film study by ellipsometry. *Optical Materials Express*. **9**, 3691 (2019).

64. R. Santbergen, R. Mishima, T. Meguro, M. Hino, H. Uzu, J. Blanker, K. Yamamoto, M. Zeman, M. A. Green, K. Emery, Y. Hishikawa, W. Warta, E. D. Dunlop, C. Ballif, J. Werner, G. Nogay, A. Walter, J. Geissbuhler, J. P. Seif, F. J. Haug, S. de Wolf, B. Niesen, C. Allebe, D. Saccetto, M. Despeisse, S. J. Moon, S. Nicolay, J. Bailat, Minimizing optical losses in monolithic perovskite/c-Si tandem solar cells with a flat top cell. *Optics Express, Vol. 24, Issue 18, pp. A1288-A1299*. **24**, A1288–A1299 (2016).

65. L. A. A. Pettersson, L. S. Roman, O. Inganas, Modeling photocurrent action spectra of photovoltaic devices based on organic thin films. *Journal of Applied Physics*. **86**, 487–496 (1999).

66. R. F. Pierret, *Advanced semiconductor fundamentals* (Prentice Hall, Upper Saddle River, N.J., 2003).

67. Taurus Medici (2010).

68. J. Huang, J. Yu, H. Lin, Y. Jiang, Detailed analysis of bathocuproine layer for organic solar cells based on copper phthalocyanine and C 60. *Journal of Applied Physics*. **105**, 073105 (2009).

69. D. Shi, X. Qin, Y. Li, Y. He, C. Zhong, J. Pan, H. Dong, W. Xu, T. Li, W. Hu, Spiro-OMeTAD single crystals: Remarkably enhanced charge-carrier transport via mesoscale ordering. *Science advances*. **2**, e1501491 (2016).

70. E. Farrell, J.-L. Brousseau, Guide for DLS sample preparation.

https://www.science.org/doi/10.1126/science.abq7652; SCIENCE 377, ISSUE 6613, PP 1425-1430 (2022) DOI: 10.1126/SCIENCE.ABQ7652

Acknowledgments

We thank Mohammad H. K. Samani, and Amanda B. Marciel for useful discussions on the DLS measurements. **Funding:** The work at Rice University was supported by the DOE-EERE 0008843 program. J.E. acknowledges the financial support from the Institut Universitaire de France. The work at ISCR and Institut FOTON was performed with funding from the European Union's Horizon 2020 research and innovation program under grant agreement no. 861985 (PeroCUBE). At Northwestern, the work was supported by the Office of Naval Research (ONR) under grant N00014-20-1-2725. This research used facilities of the Advanced Photon Source, a U.S Department of Energy (DOE) Office of Science User Facility operated for the DOE Office of Science by Argonne National Laboratory under Contract No. DE-AC02-06CH11357. ToF-SIMS analysis were carried out with support provided by the National Science Foundation CBET-1626418. This work is conducted in part using resources of the Shared Equipment Authority at Rice University. The work at the University of Washington, by K. H., R.G., and D. S. G. is supported by DOE BES under Award Number DE-SC0013957. This research used facilities and instrumentation supported by the U.S. National Science Foundation through the UW Molecular Engineering Materials Center (MEM-C), a Materials Research Science and Engineering Center (DMR-1719797). **Author contributions:** A.D.M, S.S. and J. E. conceived the idea, designed the experiments, analysed the data and co-wrote the MS. Y.W. performed 2D|3D passivation experiments. W. L. and J. S. performed GIWAX measurements, A. J. T, performed PL maps, X. T. S performed SEM and AFM imaging, A. A. helped with solar cell fabrication and characterization. M. D. performed photoluminescence measurements, M. G. K, and M. J analysed the solvation chemistry along with synthesis of 2D HaP crystals. C. K. and B. T, helped understand the 3D|2D interface with DFT modelling. A. P and P. A. performed TEM measurements. K. H, R, G and D. G. performed SKPM measurements, R. A. and M. A. A performed device modelling and optical simulations. T. T. helped perform TOF-SIMS and analyse data. All authors contributed to the MS. **Competing interests:** Rice University have filed patent for method of fabricating the 3D/PP-2D bilayer stack. **Data and materials availability:** All data are available in the main text or the supplementary materials.

SUPPLEMENTARY MATERIALS

Materials and Methods
Movie S1
Movie S2
Supplementary Text
Fig. S1 to S33
Tables S1 to S8

https://www.science.org/doi/10.1126/science.abq7652; SCIENCE 377, ISSUE 6613, PP 1425-1430 (2022) DOI: 10.1126/SCIENCE.ABQ7652

Supplementary Information

Deterministic fabrication of 3D|2D perovskite bilayer stacks for durable and efficient solar cells

Siraj Sidhik[1,2], Yafei Wang[2,3], Michael De Sienna[4], Reza Asadpour[5], Andrew Torma[6], Tanguy Terlier[7], Kevin Ho[8], Wenbin Li[2,6], Anand B. Puthirath[1], Xinting Shuai[1], Ayush Agarwal[2], Boubacar Traore[9], Matthew Jones[1,10], Rajiv Giridharagopal[8], Pulickel M. Ajayan[1], Joseph Strzalka[11], David Ginger[8], Claudine Katan[9], Muhammad Ashraful Alam[5], Jacky Even[12]*, Mercouri G. Kanatzidis[4], and Aditya D. Mohite[1,2]*

1. Methods and Characterization

1.1 Phase-selective 2D perovskite thin film formation

Step 1: High purity 2D perovskite powder synthesis: The 2D Ruddlesden popper perovskite parent-crystals of different n-values thicknesses, $BA_2MA_{n-1}Pb_nI_{3n+1}$ were synthesized using our previously reported method where lead oxide (PbO, Sigma Aldrich, 99%), methylamine hydrochloride (MACl, Sigma Aldrich, ≥98%) and butylamine (BA, Sigma Aldrich, 99.5%) was mixed in appropriate stoichiometry in a mixture of hydroiodic acid (HI, 57 wt% in H_2O) and hypophosphorous acid (H_3PO_2, 50% in H_2O). The solution was stirred to a temperature of 240˚C until all the precursors were dissolved, and the solution started boiling. Then, the precursor solution was allowed to cool down at room temperature which led to the crystallization of flat single crystals of micrometer to millimeter size. The quality and phase purity of the synthesized were verified by a combination of x-ray diffraction and absorbance measurements.

Step 2: Solution processing and film fabrication: To obtain phase-pure (PP) 2D perovskite thin films, we dissolved the high purity 2D perovskite powders in acetonitrile (MeCN, Sigma Aldrich, >99.9%) by stirring overnight at room temperature. Further 70 µl of the prepared solution was instantly dropped and spin-coated over substrates at 4000 r.p.m for 200 s followed by heating at 80°C for 3-5 min resulting in the formation of the 2D perovskite thin films.

1.2 Solar cell fabrication

Regular Planar perovskite solar cells (PSCs): The glass/FTO substrates (Kaivo Tech., < 15Ω/sq) were sequentially cleaned using soap water, water, acetone, and acetone: ethanol (1:1) by ultrasonication for 15 min. The substrates were further dried under clean dry air and left for UV-ozone for 30 min. To grow the electron transport layer (ETL), the SnO_2 colloid precursor solution obtained from Alfa Aesar (tin (IV) oxide, 15% in H_2O colloidal dispersion) was diluted by water to 2.67%, followed by spin coating at 5000 rpm

for 30 s. Further, the SnO_2 films were baked in ambient air at 150 ºC for 30 min. Before transferring it to the glove box, the ETL substrates were placed in UV-ozone for 15 min to improve the wetting properties. The triple cation (TC) perovskite solution, $Cs_5(MA_{0.10}FA_{0.90})_{95}Pb(I_{0.90}Br_{0.10})_3$ was prepared by mixing 1.09 M lead iodide (perovskite grade, TCI America), 1.0 M Formamidinium iodide (FAI, Greatcell), 0.22 M lead bromide ($PbBr_2$, Sigma Aldrich) and 0.2 M methylammonium bromide (MABr, Greatcell) in a mixture of N, N-dimethyl formamide, and dimethyl sulfoxide (DMF: DMSO, 4:1). The solution was further mixed with 5 vol% of 1.5 M cesium iodide (CsI, Sigma Aldrich) dissolved in DMSO, and left under stirring for 3 h at 70 ºC. The 70 µl of the solution was further spread in the middle of the ETL substrate and spin-coated at 1000 rpm for 10 s, and 6000 rpm for 20 s with an acceleration of 2000 rpm/s, followed by annealing at 100 ºC for 30-40 min. The 3D/PP-2D bilayer stack was fabricated using the technique described in the supplementary methods section 1.1. Following this, the spiro-MeOTAD (1-Material) acting as the hole transport layer (HTL) was spin-coated on the perovskite film at 4000 rpm for 20 s, where 1 ml Spiro-OMeTAD/chlorobenzene (90 mg ml^{-1}) solution was employed with the addition of 20 µl Li-TFSI/acetonitrile (520 mg ml^{-1}) and 34 µl tBP. Finally, the Au electrode was thermally evaporated at a pressure of $<2x10^{-6}$ torr. The active area was 0.5 cm^2.

Inverted Planar perovskite solar cells (PSCs): The patterned glass/ITO substrates were sequentially cleaned with soap water, deionized water, acetone, and acetone: ethanol (1:1) under ultrasonication for 15 min each. After drying the substrates and cleaning using the UV-ozone for 30 min, the substrates were transferred to the glove box, where an HTL of ~8 nm thickness was made of poly(triarylamine) (PTAA, Sigma Aldrich) with a concentration of 2 mg/ml in chlorobenzene by spin coating at 6000 rpm for 30 s, followed by annealing at 150 ˚C for 10 min. The TC perovskite precursor solution of 1.5 M was prepared by mixing PbI_2, FAI, MABr, $PbBr_2$, and CsI in a mixed solvent of DMF and DMSO (4:1), to obtain a composition of $Cs_5(MA_{0.10}FA_{0.90})_{95}Pb(I_{0.90}Br_{0.10})_3$. A two-step spin-coating protocol of 1000 rpm for 10 s and 6000 rpm for 20 s with an acceleration of 2000 rpm/s was utilized to obtain uniform coverage of the perovskite film. The samples were further annealed at 100 ˚C for 30-40 min. The 3D/PP-2D bilayer stack was fabricated using the technique described in the supplementary methods section 1.1. Finally, the devices were completed by thermally evaporating C60 (30 nm), BCP (1 nm), and Copper (100 nm) under a vacuum of $<2x10^{-6}$ torr. The active area chosen was 0.5 cm^2.

1.3 Optical absorbance and photoluminescence measurements

Thin-film photoluminescence (PL): Steady-State Photoluminescence (SS-PL) was acquired through a lab-built confocal microscopy system. Spectra were collected using a spectrometer (Andor Kymera 329i) and a CCD (Andor iDus 416), then fit using a Savitzky-Golay filtering. The samples were photo-excited at 2.58 eV (480 nm) using a monochromatic pulsed laser (6ps pulse, repetition rate 78.1 MHz, NKT Photonics SuperK Fianium) focused near diffraction limit (~0.5um resolution) with excitation intensity

tuned at 360 W/cm^2. Data were collected from 450 - 900 nm using a dwell time of 0.1 s with samples under vacuum (10^{-5} torr) at room temperature. PL maps were measured for a 40 μm x 40 μm region or a 100 μm x 100 μm with a step size of 1 μm, where the peak position was extracted at each step.

Thin-film absorbance: Film absorbance measurements were performed by illuminating the samples with monochromatic light modulated at 2 kHz coming from a quartz-tungsten-halogen light source fed into a monochromator (SpectraPro HRS 300, Princeton instruments). Synchronous detection of the transmitted light was achieved with a silicon photodiode hooked to an SR865 lock-in amplifier. Data was collected from 400 – 800 nm using a dwell time of 0.1 s. During all measurements, the samples were kept under a vacuum (~10^{-4} torr) and at room temperature.

1.4 Steady-state PL and Time-resolved photoluminescence (TRPL) measurements

Steady-state PL: Steady-State PL was acquired on 3D and 3D/2D HaP bilayer stack deposited on ITO/SnO2 substrate using Edinburgh Instruments FLS1000 spectrophotometer with a 450 W ozone-free Xenon arc lamp. The samples were excited on the perovskite side. The excitation and emission bandwidths are 5 and 2 nm, respectively.

Time-resolved PL: The TRPL of the 3D and 3D/2D perovskite film deposited on the ITO/SnO_2 substrate was measured using a time-correlated single-photon counting (TCSPC) spectrophotometer (Edinburgh Instruments FLS1000). The sample was excited by a 405 nm pulsed laser (60 μW/cm^2 at 1 MHz repetition rate) on the perovskite side, and the time-resolved emission was collected at the peak of the PL. The obtained TRPL decay was fitted using a tri-exponential function and convoluted with the instrument response function (IRF). The carrier lifetime of each of the samples was calculated based on a weighted average of the fitted decay**.**

1.5 X-ray diffraction measurements

The x-ray diffraction of the 3D and 3D/2D perovskite thin films was measured in the 2θ between 3^o and 32^o, with a step of 0.01^o and a speed of 2 degrees per minute, using a Rigaku SmartLab X-Ray diffractometer with Cu(K$\boldsymbol{\alpha}$) radiation (λ = 1.5406 Å).

1.6 Time-of-Flight Secondary Ion Mass Spectrometry (ToF-SIMS) measurements

Positive high mass resolution depth profiles were performed using a ToF-SIMS NCS instrument, which combines a TOF.SIMS instrument (ION-TOF GmbH, Münster, Germany) and an in-situ Scanning Probe Microscope (NanoScan, Switzerland) at Shared Equipment Authority from Rice University. The analysis field of view was 80 × 80 μm^2 (Bi_3^+ @ 30 keV, 0.35 pA) with a raster of 128 x 128 along with the depth profile. A charge compensation with an electron flood gun has been applied during the analysis. An adjustment of the charge effects has been operated using a surface potential of -36V and an extraction bias of 0V. The cycle times was fixed to 90 μs (corresponding to m/z = 0– 735 a.m.u mass range). The sputtering raster was 450 × 450 μm^2 (Cs^+ @ 1 keV, 44 nA). The beams were operated in non-interlaced mode, alternating 1 analysis cycle and 1 frame of sputtering

(corresponding to 1.31s) followed by a pause of 2 s for the charge compensation. The MCs_n^+ ($n = 1, 2$) depth profiling has also been used to improve the understanding of the data. This is a useful method, mainly applied to quantify the alloys but also to identify any ion compounds. The cesium primary beam is used for sputtering during the depth profile and permits the detection of MCs^+ or MCs_2^+ cluster ions where M is the element of interest combined with one or two Cs atoms. The advantages of following MCs^+ and MCs_2^+ ions during ToF-SIMS analysis include reducing matrix effects and the possibility of detecting the compounds from both electronegative and electropositive elements and compounds. All depth profiles have been point-to-point normalized by the total ion intensity and the data have been plotted using a 5-points adjacent averaging. Both normalization and smoothing have permitted a better comparison of the data from the different samples. The depth calibrations have been established based on the measured thicknesses using the surface profiler to obtain a line scan of the craters with the *in-situ* SPM by contact scanning.

1.8 Grazing incidence wide-angle x-ray scattering (GIWAXS)

Experimental methods: All synchrotron GIWAXS patterns used in this paper were measured at beamline 8-ID-E at the Advanced Photon Source (APS)(*40*). Samples were mounted on a custom grazing incident scattering sample wheel and were measured inside a vacuum chamber (10^{-4} torr) to prevent degradation. The Pilatus 1M (Dectris) area detector was 217mm away from the sample. The X-ray beam energy was 10.91keV and the beam size was $200\mu m$ x $20\mu m$ (Height vs Vertical). All GIWAXS patterns were corrected with experimental conditions (detector sensitivity, X-ray polarization, and geometrical solid-angle parameters)(*41*). The GIWAXS patterns were processed using the GIXSGUI package running on Matlab 2018b.

GIWAXS Analysis: To analyse the GIWAXS patterns, we performed a full angular integration to extract a 1-D X-ray spectrum. We used the Debye-Scherrer formula to extract the average grain size (D_{hkl}) of the 2D/3D perovskite thin film (hkl is the miller indices)(*42*). The (020) plane was used for the analysis of the 2D perovskite top film and the (001) plane was used for the 3D perovskite film. A shape factor (K) of 0.9 was used in the Scherrer equation. The formula is given as the following

$$D_{hkl} = \frac{K\lambda}{\beta_{hkl}\cos\theta_{hkl}} \quad (1)$$

where λ is 1.1365 Å and is the X-ray wavelength, θ is the diffraction peak position, β is the full-with-at-half-max (FWHM). The FWHM was extracted by fitting the diffraction profile to a pseudo-Voigt function(*43*). The FWHM was correct for the measurement geometry such as the X-ray beam divergence, energy bandwidth, and the parallax effect of the beam footprint (*44*).

Penetration depth curve: The penetration depth calculation was performed by using the GIXA calculator in https://gixa.ati.tuwien.ac.at/tools/penetrationdepth.xhtml. Here we

use the materials constants of the **Z**, average atomic number, **A**, average atomic mass (g/mol), **p**, mass density (g./cm^3), and **μ**, the linear attenuation coefficient.

1.10 Scanning Kelvin probe microscopy measurements

Surface photovoltage measurements: Scanning Kelvin probe microscopy (SKPM) experiments were performed using an Asylum Research MFP-3D atomic force microscope (AFM) mounted on an inverted Nikon Eclipse microscope. The tips used were Pt-coated silicon tips (MikroMasch HQ: NSC15/Pt, 325 kHz, and 40 N/m). All measurements were collected using a flow cell in a nitrogen environment. Amplitude modulated (AM) SKPM was used with a lift height of 30 nm. For surface photovoltage (SPV) measurements, the samples were illuminated from the bottom (glass side) using a 590 nm orange LED (2.39 mW/cm^2) with the LED spot focused on the surface and co-aligned with the tip. SKPM images were collected in the dark and under illumination in the same area, and the CPD values were allowed to equilibrate before they were used to determine the SPV. This process was repeated for at least three 4 x 4 μm^2 areas used for averaging. Here, we use the convention where CPD is equal to the sign of the voltage on the tip, meaning a more positive CPD corresponds to a smaller work function (closer to vacuum).

1.10 Dynamic Light Scattering (DLS) measurements

Experimental methods: The 2D perovskite solutions were prepared by dissolving different concentrations of synthesized high purity crystal powders in MeCN and loading them into the cylindrical glass cuvettes (3mm diameter, LS Instruments AG, Fribourg). The DLS measurements were immediately carried out by measuring the correlation curves in five different directions, corresponding to the angles 30°, 60°, 90°, 120°, 150° (or at a single angle over ~ 40 hrs), with respect to the incident laser beam at an ambient temperature of 21°C using a fully automated 3D LS Spectrometer (LASER: 660 nm, 65 mW, LS Instruments AG, Fribourg).

Extraction of the size of the particles in solution: The analysis of the multi-angle DLS data obtained for different concentrations of precursor solutions are detailed below. The angular dependence of the autocorrelation curve was measured for each solution. The obtained correlation curves were fitted using a single-exponential decay model. Also, the resulting correlation fitting residuals were calculated and plotted followed by linear regression of Γ vs q^2 between 30° and 150°.

The scattered light correlation function, $g^{(2)}$, compares the intensity of the received signal between time t and later time t+τ,(*45*)

$$g^{(2)}(q,\tau) = \frac{<I(t)I(t+\tau)>}{<I(t)^2>} \quad (2)$$

We use the Siegert relationship to relate the intensity correlation function and the field correlation function which is given (*45*)

$$g^{(2)}(q,\tau) - 1 = \beta\left|g^{(1)}(q,\tau)\right|^2 \quad (3)$$

where β is a constant proportional to the signal-to-noise ratio.

For a system undergoing Brownian motion, the electric field correlation function is shown to decay exponentially as

$$g^{(1)}(q,\tau) = \exp(-\Gamma\tau) \tag{4}$$

For several groups of particles with different sizes (labeled as i) are present in the solution, the DLS data can be fitted using(*46*):

$$g^{(2)}(q,\tau) - 1 = \sum_i \alpha_i \left| g_i^{(1)}(q,\tau) \right|^2 = \sum_i \alpha_i \left| \exp(-\Gamma_i \tau) \right|^2 \tag{5}$$

Then, for the group of particles i the value Γ_i is related to the translational diffusion coefficient $D_{T,i}$ and wave number q through

$$\Gamma_i = D_{T,i} q^2 \tag{6}$$

with,

$$q = \frac{4\pi\eta}{\lambda} \sin\left(\frac{\theta}{2}\right) \tag{7}$$

η is the refractive index of the solvent, λ is the wavelength of the laser, and θ is the angle between the incident laser beam and the scattered light. Finally, the diffusion coefficient is related to the hydrodynamic radius R_{H} of particles in a Brownian motion by the Stokes-Einstein equation(*47*)

$$D_{T,i} = \frac{k_{\mathrm{B}} T}{6\pi\mu R_{\mathrm{H},i}} \tag{8}$$

with k_{B} is the Boltzmann constant, T the temperature, μ the dynamic viscosity, and $R_{H,i}$ the median hydrodynamic radius of the group i of particles.

1.11 Thin-film morphology measurements

Scanning electron microscopy (SEM) measurements: The surficial and cross-sectional SEM images were recorded using FEI Quanta 400 ESEM FEG. The 3D control and the 3D/2D perovskite films were fabricated on the Silicon substrate, followed by sputtering of □15 nm gold to enhance the conductivity of the films. The images were collected at a voltage of 12.5 kV with a dwell time of 30 μs.

Atomic force microscopy (AFM) measurements: The AFM measurements were performed using NX20 AFM (Park systems). The surface topographical images were obtained in tapping mode using a silicon tip at a resonant frequency of 300 kHz and a the spring constant of 26 N/m. The root mean square (RMS) roughness values were extracted from an image of 5μm x 5μm.

Transmission electron microscopy (TEM) measurements: The TEM specimen of the PVSKT sample was prepared via a focused ion beam milling process employing a Helios NanoLab 660

FIB unit and an aberration-corrected Titan Transmission electron microscope (FEI Titan Themis 3) with an acceleration voltage of 300 kV was used to perform the electron microscopy.

1.12 Determination of electronic band levels using Photoemission yield spectroscopy (PES)

The PES (AC-2, Riken-Keiki) measurements were used to obtain the valance band maximum (VBM) of the 3D, 2D ($BA_2MA_2Pb_3I_{10}$, Ruddlesden-popper), and 3D/2D perovskite. The samples were illuminated by a monochromatic ultra-violet (UV) light under ambient conditions. The UV photon with energy higher than the ionization energy (I.E) of the sample to be measured, was used to ionize an electron to the vacuum level. This electron can ionize a gas molecule in proximity to the surface which is measured by the detector. For a typical measurement, the energy of the photons varies between 4.2 eV to 6.2 eV, and the number of generated photoelectrons is measured for each energy. This value is corrected according to the intensity spectrum of the UV lamp. For semiconductors, the number of photo-generated electrons near the VBM generally increases as a cube root of the energy. Hence the cube root of the corrected PYSA spectrum is plotted against the photon energy. The linear region of the plot above the onset is fitted to find the VBM, at the crossing of the linear fit and the background level. The conduction band minimum (CBM) with respect to the vacuum level (electron affinity (EA)), is calculated by subtracting the measured bandgap from the ionization energy.

1.13 DFT simulation for band alignments of 3D/2D heterostructure

DFT-based(*48*) calculations were performed using SIESTA (*49*) with a basis set of finite-range of numerical atomic orbitals. For structural optimization, we used the van der Waals density functional with C09 exchange(*50*) within the van der Waals DF2 flavor to describe the exchange-correlation term (we modified SIESTA version "master-post-4.1-251" to include DF2 flavor). This tuning was suggested to improve C09-based geometry optimization over that with the original DF1 flavor(*51*). The latter has already proven to provide a good description of experimental lattice constants similar to those obtained with optimized GGA-based PBEsol functional in solids(*52*). Norm-conserving Troullier-Martins pseudopotentials were used for each atomic species to account for the core electrons(*53*). $1s^1$, $2s^22p^2$, $2s^22p^3$, $5s^25p^5$ and $5d^{10}6s^26p^2$ $3s^23p^4$ were used as valence electrons for H, C, N, I, Pb respectively. A Polarized Double-zeta (DZP) basis set with an energy shift of 200 meV and a real space mesh grid energy cut-off of 400 Rydberg were used for the calculations. We used 8x8x8 and 4x4x1 Monkhorst-Pack k-point grids for the bulk and heterostructure systems, respectively.

For band alignments, we used single-point calculations with GGA-PBE functional combined with DFT-1/2, including spin-orbit coupling on top of vdwDF2-C09 optimized structures(*54*). Spin-orbit coupling (SOC), when used, was considered in its on-site approximation as proposed by Fernàndez-Seivane *et* al.(*55*).

For the heterostructure construction, we used the doubled cubic cells in the plane of the perovskite to lattice match it to the 2D layer cell. This cell doubling corresponds to multiplying the cubic lattice constant by $\sqrt{2}$ ($a_{hetero} = \sqrt{2}\, a_{bulk}$). For the heterostructure using 2D-based BA, we used the room-temperature structure of BA_2PbI_4 (*56*). For the n=2-4, we used the structures reported in Ref. (*57*). We considered 9 octahedral layers for the 3D $FA^{Cs}PbI_3$(FA^{Cs} = FA replaced with Cs) to mimic the 3D part of the heterostructure(*58*). The in-plane lattice constants of the 3D part were imposed for the whole heterostructure and were not allowed to relax during the 2D/3D interface geometry optimization. We only allowed the c-lattice constant along z to relax along with the atomic positions. Moreover, the two surface octahedral layers of the 3D perovskite part were allowed to relax while keeping the bulk-like regions frozen to the positions of the optimized bulk structure. This strategy allows capture of the surface effects during the relaxation while maintaining the integrity of the bulk region of heterostructures, which is useful for the energy level alignment. We used the fast-inertial relaxation engine (FIRE) algorithm(*59*) for the different relaxations and the maximum force was set to 0.06 eV/Å.

For the absolute valence energy level alignment, we constructed slabs from the experimental bulk structures for both 2D and 3D systems. $FA^{Cs}PbI_3$ was used for the 3D slab while the Ruddlesden-Popper phase n=1-4 was used for the 2D. The absolute valence energy levels of the different systems were computed using the Hartree potential alignment with the vacuum level set as the reference. Here, the absolute valence energy level $E_v^{abs}$is obtained using:

$$E_v^{abs} = VBM_{bulk} + \Delta V_H + \Delta E_{vacuum} \quad (9)$$

where VBM_{bulk} is the valence band maximum of the bulk system, $\Delta V_H = V_H^{slab} - V_H^{bulk}$ is the shift of the Hartree potential between the slab and the bulk systems, and $\Delta E_{vacuum} = 0 - E_{vacuum}$ is the vacuum level shift with respect to zero energy level. VBM_{bulk} is corrected using the DFT-1/2 method. For the conduction band, we added to E_v^{abs} the experimentally reported electronic band gaps. This then gives,

$$E_c^{abs} = E_v^{abs} + E_g^{exp} \quad (10)$$

1.14 Solar cell devices characterization

Solar cell performances: The performances of the solar cells were obtained by measuring the current-voltage (J-V) curves of each device illuminated by an ABB solar simulator from Newport (model 94011). The arc simulator modeled AM 1.5G irradiance of 100 mW/cm^2 whose intensity was calibrated using a NIST-certified Si solar cell (Newport 91150V, ISO 17025) and corrected by measuring the spectral mismatch between the solar spectrum, reference cell, and the spectral response of the PV device. We estimate a mismatch factor of 3%. The solar cells were measured with a Keithley 2401 instrument from 1.2 to 0 V and back, with a step size of 0.05 V and a dwell time of 0.1 s, after light soaking for 10 s. The defined active area was 0.5 cm^2.

External quantum efficiency: The external quantum efficiency (EQE) of the solar cell devices was collected by first illuminating each device with monochromatic light modulated at 2 kHz coming from a quartz-tungsten-halogen light source fed into a monochromator (SpectraPro HRS 300, Princeton instruments). The photocurrent response of the solar cells was measured by an SR865 lock-in amplifier. The light source spectrum response was calibrated using a calibrated silicon diode (FDS1010, Thorlabs).

Stability tests: For stability test measurements, the perovskite devices were encapsulated with a UV- curable epoxy (Poland Inc.) and a glass coverslip as a barrier layer in an argon-filled glove box. Argon gas was blown over the devices to remove any contaminants or dust particles just before encapsulation. All the devices were tested at the continuous maximum power point condition, under full-spectrum simulated AM 1.5G (100 mA cm^{-2} irradiance) in the air using an ABB solar simulator (94011A, Newport) – ISOS-L1 protocol. Each data point was collected after an interval of 15 min. The relative humidity was measured to be constant at 70 ± 5 %RH and the operating temperature was 60± 5 ˚C.

1.15 Device simulation

*Optical Modelling***:** Optical absorption in different layers of the PV cell is calculated by the full-wave solution of Maxwell's equations with the input of AM 1.5G illumination. The materials in different layers of the cell are characterized by absorption coefficient and refractive indices that are obtained from the literature (*60*–*64*) or measured data by the authors. Transfer matrix method (TMM) (*65*) calculations are used for the optical studies of the planar cell structure. In this approach, the entire solar cell stack, including the contact layers, is modeled using a series of interface and phase matrices. The central quantity which is calculated in this approach is the point-wise optical absorbance [A(λ,r)] inside various layers of the cell. The wavelength range of 300-1500 nm has been used for our calculations (see Fig. S26A-D). The spatially resolved absorption profile is integrated over the wavelength range to create the generation profile for the electron and holes for self-consistent carrier transport simulation as described below.

Self-consistent transport simulation: The transport of charged carriers (electrons and holes) is modeled by generalized drift-diffusion formalism (*66*). Photo-generation is calculated from the optical absorption profile (integrated over the wavelengths) discussed previously. The electron and hole transport inside the cell is stimulated by a self-consistent solution of Poisson and continuity equations by a commercial-grade device simulator MEIDCI™ (*67*) The generation term in the e–h continuity equations is calculated from the solution of a photo-generated profile. The recombination term in continuity consists of direct and Shockley-Read-Hall (SRH) recombination with lifetime found in the literature. We do not account for hot electron effects. The excitons – if any – are presumed to dissociate into free electron and hole pairs immediately after generation.

For all the simulations (including different thicknesses), we consider four quantum wells for the 2D perovskite layer throughout the film thickness, which gives 4 lower bandgap wells along with 5 high bandgap barriers. We assume the distance of those potential wells

is uniformly distributed in the model. The thickness of each potential well is thus the thickness of full film divided by nine. For example, for perovskite thickness of 45 nm, 30 nm, 18 nm, 6 nm, the thickness of quantum well is 5 nm, 3.33 nm, 2 nm, 0.66 nm, respectively.

See Table S1 for model equations and see Table S2 to S7 for simulation parameters. The parameters with references are taken from the literature; the rest are assumed to match the data for 2D and 3D perovskite layers. To follow the trend of experimental results we used quantum wells with a depth of 35 meV at both conduction and valence band. Therefore, the bandgap in the quantum well is 70 meV lower than the outside.

We note that optical simulations do not account for the variations in microstructural properties such as interface roughness, orientation, and film morphology in solving this model.

Table S1. Equations used for carrier transport simulation(66)

Poisson Equation:

$$\epsilon_r \epsilon_0 \nabla^2 \psi = -q\,(n_h - n_e)$$

Continuity:

$$\nabla J_{e,h} = \left(G_{e,h} - R_{e,h}(n_e, n_h)\right)$$

Drift-Diffusion:

$$J_{e,h} = \mu_{e,h} n_{e,h}(-\nabla\psi) \pm D_{e,h}\nabla n_{e,h}$$

Recombination:

$$R_{e,h}(n_e, n_h) = B(n_e n_h - n_i^2) + \frac{n_e n_h - n_i^2}{\tau(n_e + n_h)}$$

Table S2. Optoelectronic parameters for $BA_2MAPb_3I_{10}$ 2D perovskite absorber (n=3)(60)

Symbol	**Description**	**Parameter value**
$L_{Absorber}$	The thickness of the absorber layer	0 to 45 nm (variable)

μ_e	Electron mobility in the absorber	0.1 (cm^2/V. s)
μ_h	Hole mobility in the absorber	0.1 (cm^2/V. s)
τ_e	Electron lifetime in the absorber	1 (ns)
τ_h	Hole lifetime in the absorber	1 (ns)
$LUMO$	Lowest Unoccupied Molecular Orbital	3.33 (eV)
E_G	The bandgap of absorber	2.03 (eV)
ε_r	Relative dielectric constant	25
N_A	Self-Doping concentration (P-type)	$1 * 10^{16}$ (#/cm^3)

Table S3. Optoelectronic parameters for, $Cs_5(MA_{0.10}FA_{0.90})_{95}Pb(I_{0.90}Br_{0.10})_3$ 3D perovskite absorber (*61*)**.**

Symbol	**Description**	**Parameter value**

$L_{Absorber}$	The thickness of the absorber layer	450 nm
μ_e	Electron mobility in absorber	10 (cm^2/V.s)
μ_h	Hole mobility in the absorber	10 (cm^2/V.s)
τ_e	Electron lifetime in the absorber	50 (ns)
τ_h	Hole lifetime in the absorber	50 (ns)
$LUMO$	Lowest Unoccupied Molecular Orbital	3.79 (eV)
E_G	The bandgap of absorber	1.60 (eV)
ε_r	Relative dielectric constant	25
N_A	Self-Doping concentration (P-type)	10^{16} (#/cm^3)

Table S4. Optoelectronic parameters for the hole transport material (HTM), PTAA used in the p-i-n photovoltaic (PV) device(*64*)**.**

Symbol	**Description**	**Parameter value**

L_{HTM}	The thickness of the HTM layer	20 nm
μ_e	Electron mobility in HTM	$1 * 10^{-3}$ (cm^2/V.s)
μ_h	Hole mobility in HTM	$1 * 10^{-3}$ (cm^2/V.s)
τ_e	Electron lifetime in HTM	1000 (ns)
τ_h	Hole lifetime in HTM	1000 (ns)
$HUMO$	Highest Occupied Molecular Orbital	5.14 (eV)
E_G	Band gap of HTM	3.4 (eV)
ε_r	Relative dielectric constant	3
N_A	Self-Doping concentration (P-type)	$3 * 10^{17}$ (#/cm^3)

Table S5. Optoelectronic parameters for the electron transport material (ETM), C60 used in the p-i-n PV device(*68*).

Symbol	Description	Parameter value
L_{ETM}	The thickness of the ETM layer	30 nm
μ_e	Electron mobility in ETM	10^{-2} ($cm^2/V.s$)
μ_h	Hole mobility in ETM	10^{-2} $(cm^2/V.s)$
τ_e	Electron lifetime in ETM	1000 (ns)
τ_h	Hole lifetime in ETM	1000 (ns)
$LUMO$	Lowest Unoccupied Molecular Orbital	3.82 (eV)
E_G	The bandgap of ETM	1.7 (eV)
ε_r	Relative dielectric constant	4
N_D	Self-Doping concentration (N-type)	$5 * 10^{17}$ ($\#/cm^3$)

Table S6. Optoelectronic parameters for the HTM, spiro-OMeTAD used in the n-i-p PV device(*69*).

Symbol	Description	Parameter value
L_{HTM}	The thickness of the HTM layer	150 nm
μ_e	Electron mobility in HTM	$2 * 10^{-6}$ (cm^2/V.s)
μ_h	Hole mobility in HTM	$2 * 10^{-6}$ (cm^2/V.s)
τ_e	Electron lifetime in HTM	1000 (ns)
τ_h	Hole lifetime in HTM	1000 (ns)
$HUMO$	Highest Occupied Molecular Orbital	5.09 (eV)
E_G	Band gap of HTM	3.24 (eV)
ε_r	Relative dielectric constant	3
N_A	Self-Doping concentration (P-type)	$3 * 10^{19}$ (#/cm^3)

Table S7. Optoelectronic parameters for the ETM, SnO_2 used in the n-i-p PV device(*63*).

Symbol	Description	Parameter value
L_{ETM}	The thickness of the ETM layer	50 nm
μ_e	Electron mobility in ETM	10^{-2} (cm^2/V.s)
μ_h	Hole mobility in ETM	10^{-2} (cm^2/V.s)
τ_e	Electron lifetime in ETM	1000 (ns)
τ_h	Hole lifetime in ETM	1000 (ns)
$LUMO$	Lowest Unoccupied Molecular Orbital	4.00 (eV)
E_G	Band gap of ETM	3.6 (eV)
ε_r	Relative dielectric constant	4
N_D	Self-Doping concentration (N-type)	$5 * 10^{18}$ (#/cm^3)

Table S8. Optoelectronic parameters of the tunneling barrier Bathocuproine (BCP) used in the p-i-n PV device(*68*).

Symbol	Description	Parameter value
L_{ETM}	The thickness of the ETM layer	1 nm
μ_e	Electron mobility in ETM	10^{-2} (cm^2/V.s)
μ_h	Hole mobility in ETM	10^{-2} (cm^2/V.s)
τ_e	Electron lifetime in ETM	1000 (ns)
τ_h	Hole lifetime in ETM	1000 (ns)
$LUMO$	Lowest Unoccupied Molecular Orbital	3.82 (eV)
E_G	The bandgap of ETM	1.7 (eV)
ε_r	Relative dielectric constant	4
N_D	Self-Doping concentration (N-type)	$5 * 10^{17}$ (#/cm^3)

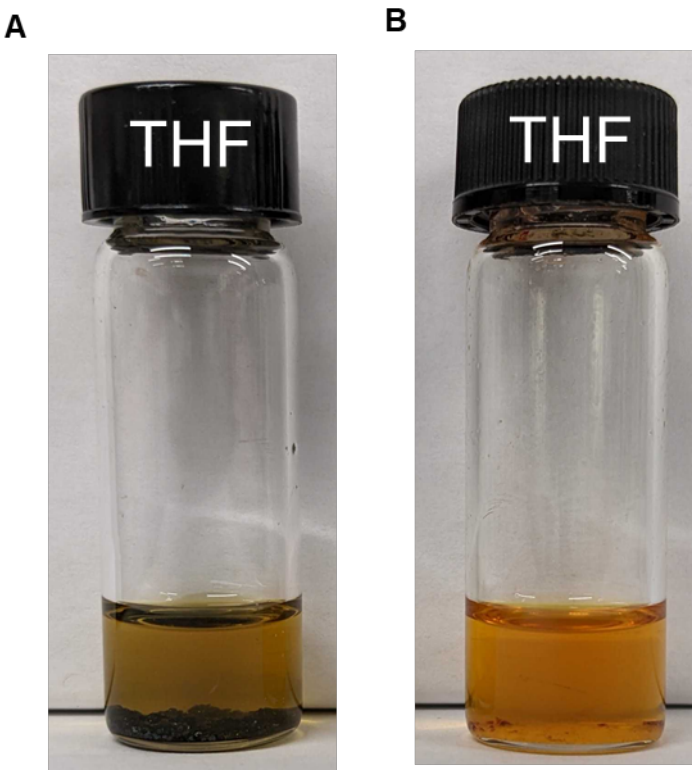

Figure S1. Photographs of vials showing A. 3D perovskite, and B. 2D perovskite powder dispersed in the solvent tetrahydrofuran (THF) not forming a stable solution.

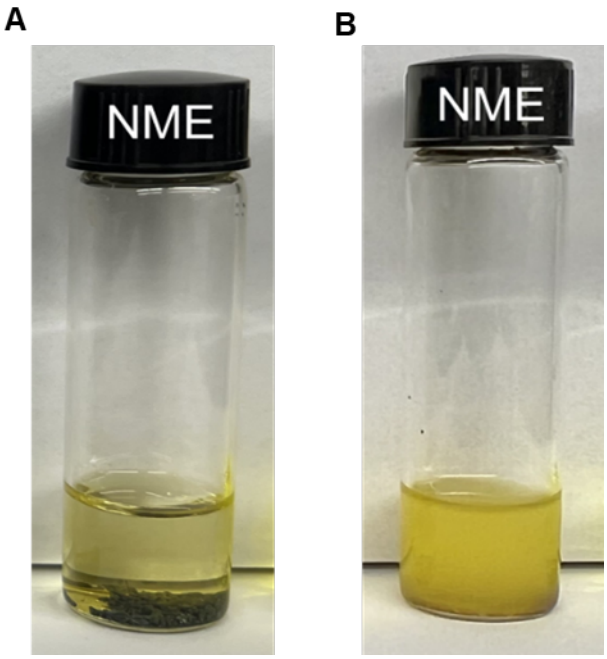

Figure S2. Photographs of vials showing A. 3D perovskite, and B. 2D perovskite powder dispersed in the solvent nitromethane (NME) not forming a stable solution.

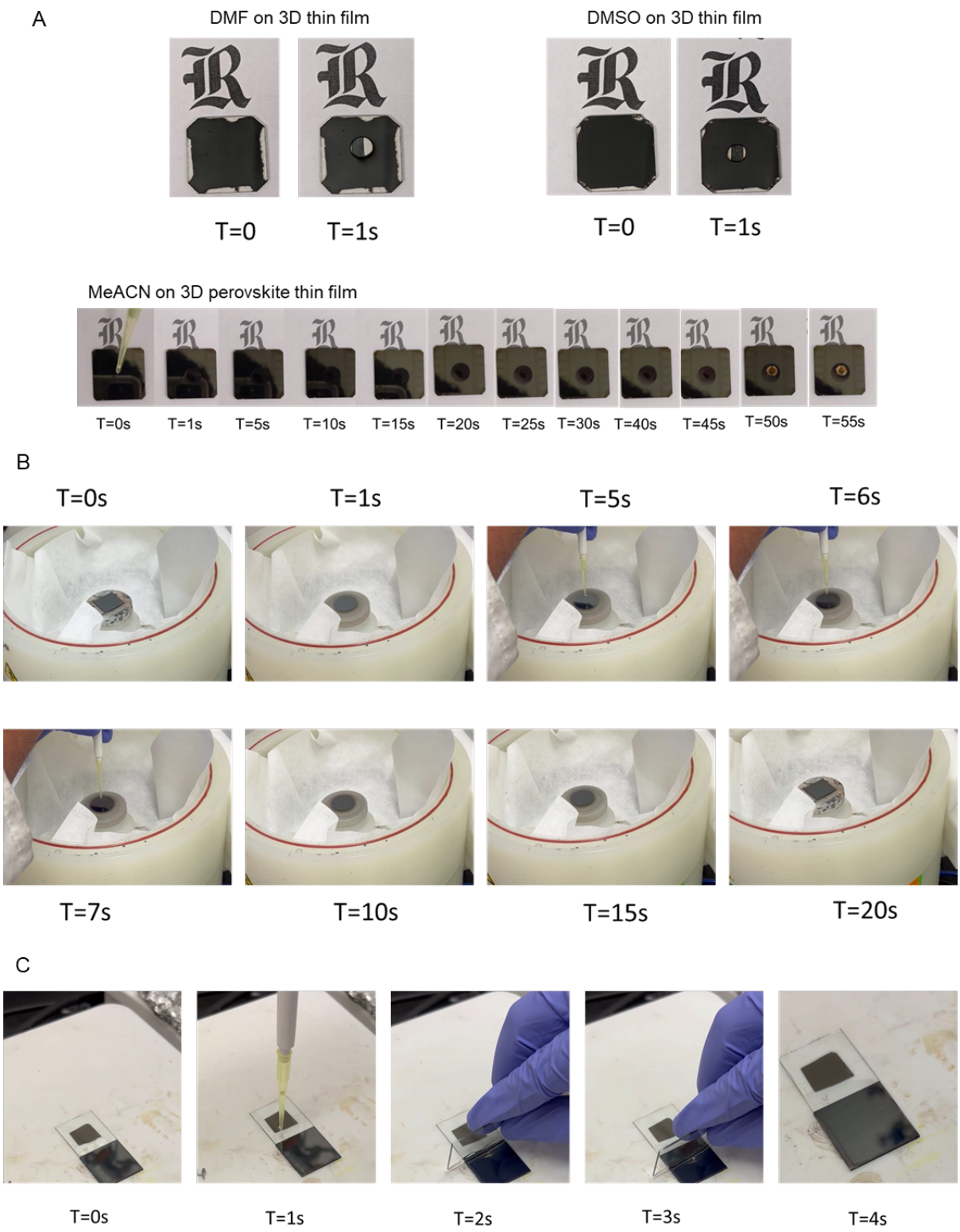

Figure S3. Photographs of the drop test that's are performed to check the solvent compatibility for forming a 3D/2D perovskite heterostructure film by A. dropping 20-30µl of the solvent on the 3D perovskite thin film, B. spincoating 100µl of of MeCN on the 3D perovskite thin film, C. blade coating 100 µl of MeCN on the 3D perovskite film.

Supplementary Note 1

To get a true sense of the solvent incompatibility in obtaining a 3D/2D HaP bilayer structure, we performed a drop test, where we introduced 20-30 µl of different solvents that forms a stable 2D perovskite solution, on top of the 3D film (with a thickness of □450-500 nm). As observed in **Fig. S3**, the solvents DMF, DMSO instantly dissolves the 3D perovskite film in 1-2 seconds making it impossible for a 2D film growth, while the MeCN takes more than 45 sec to show a recognizable change to the 3D perovskite film underneath, which is more than enough to solution-process a 2D perovskite layer on the 3D film. A closer observation showed that the MeCN just peels off the perovskite material from the substrate (leaving black perovskite powders floating) rather than dissolving it, which could be due to small thickness of the film, or poor contact with the substrate. The optoelectronic quality of the 3D perovskite film post-MeCN treatment was measured using absorption, photoluminescence, and X-ray diffraction (**see Fig. S4**), which shows no variation in the 3D perovskite film characteristics.

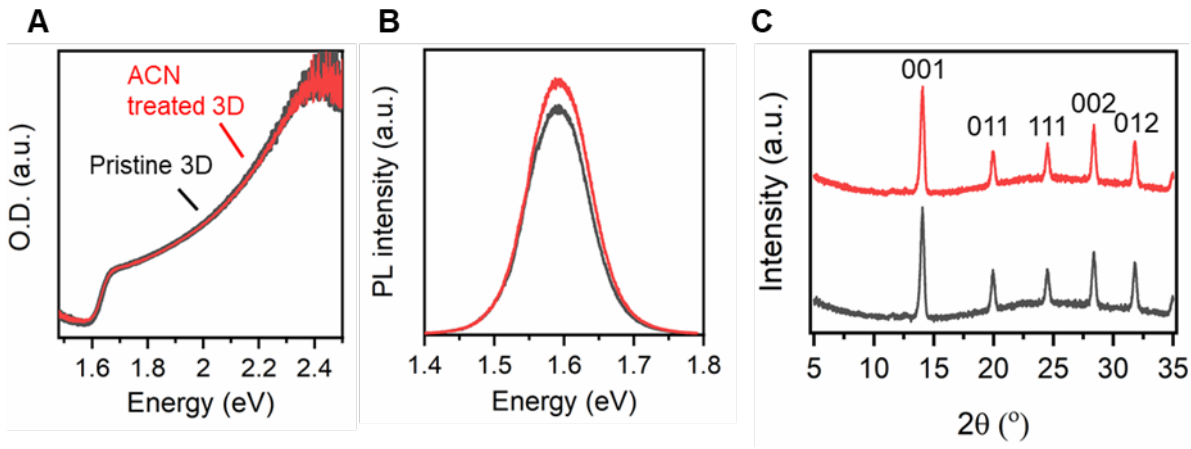

Figure S4. Plots depicting the A. absorption, B. steady-state photoluminescence, and C. X-ray diffraction spectra of the 3D perovskite film without and with acetonitrile treatment show no degradation of the 3D layer.

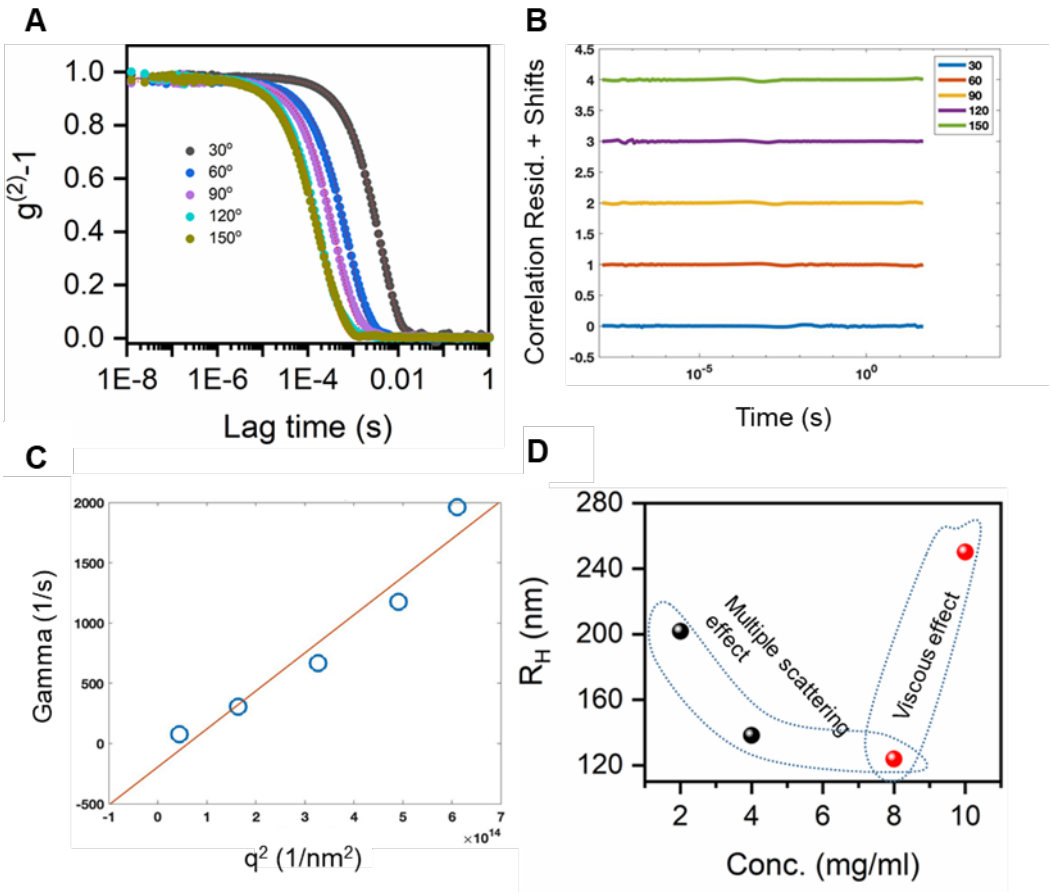

Figure S5. Size determination by dynamic light scattering of particles present in the 2D perovskite solution in MeCN. A. Correlation function ($g^{(2)}$) versus lag time (s) measured at several scattering angles. The lines correspond to the fit of the data, B. Residual of the fit functions, C. Corresponding linear regression of the Gamma values (Γ) derived from the fit to the data, D. Plot showing the change in particle size as a function of the concentration of 2D perovskite in MeCN.

Supplementary Note 2

The differences in solubility of 2D perovskites prompted us to observe the 2D perovskite solution in MeCN closely. The dynamic light scattering measurements show a uniform distribution of undissolved seeds with a relative size distribution of 100-150 nm (see Fig. S5). This indicates that the acetonitrile does not disintegrate the 2D perovskite crystal into ions of its precursors, but rather just reduces it to small units. This is consistent with our recent work, which showed that these seeds retain the memory of their parent 2D perovskite crystal powders and dictate the crystallization of dominantly phase-pure films with a homogenous bandgap(*26*).

Multiple scattering effects and viscous effects on photon correlation spectroscopy

Hydrodynamic particle size in DLS measurements is derived by,

$$R_H = \frac{kT}{6\pi\eta D} \quad (11)$$

Where R_H represents hydrodynamic radius, k the Boltzmann constant, T the temperature, η the solvent viscosity, and D the translational diffusion coefficient.

Multiple Scattering: At concentrations higher than the dilute regime where interparticle interactions happen and cannot be ignored, the incident light passes through multiple particles on its way to the detector. This results in a higher reported diffusion coefficient as the photon perceives the multi-scattering of the light as the existence of a single particle with high diffusion whereas it is the scattering of multiple particles. The high diffusion coefficients will falsely result in lower hydrodynamic radii so in this region the size will show a decreasing trend while particle sizes are unchanged(45).

Viscous Effects: As concentrations increase to higher levels, the high number of dissolved particles causes the viscosity of the solvent to increase. The increased viscosity results in slower motion of particles and increased calculated hydrodynamic radius. Note that for viscosity in Eq. 11, we always use pure solvent viscosity so that value remains constant in our calculations, but solution viscosity is way above the value of pure solvent viscosity because of high concentrations(*70*)

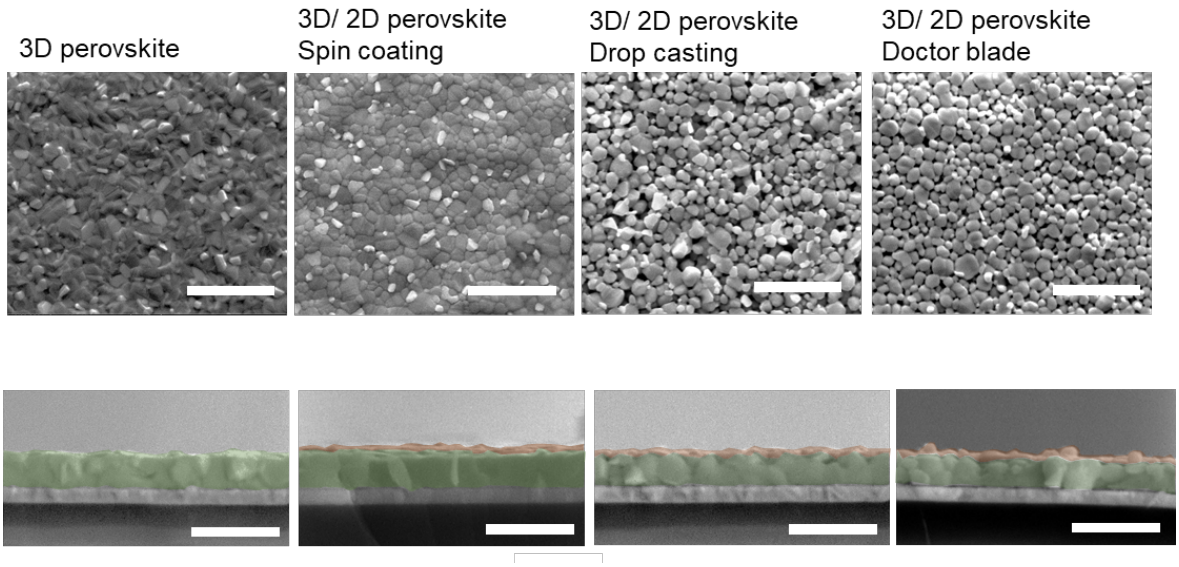

Figure S6. Surficial and cross-sectional SEM images of the 3D/2D heterostructure without and with the 2D perovskite layer grown using different deposition techniques. The green shade represents 3D and the brown shade shows the 2D layer. The scale bar is 2 μm.

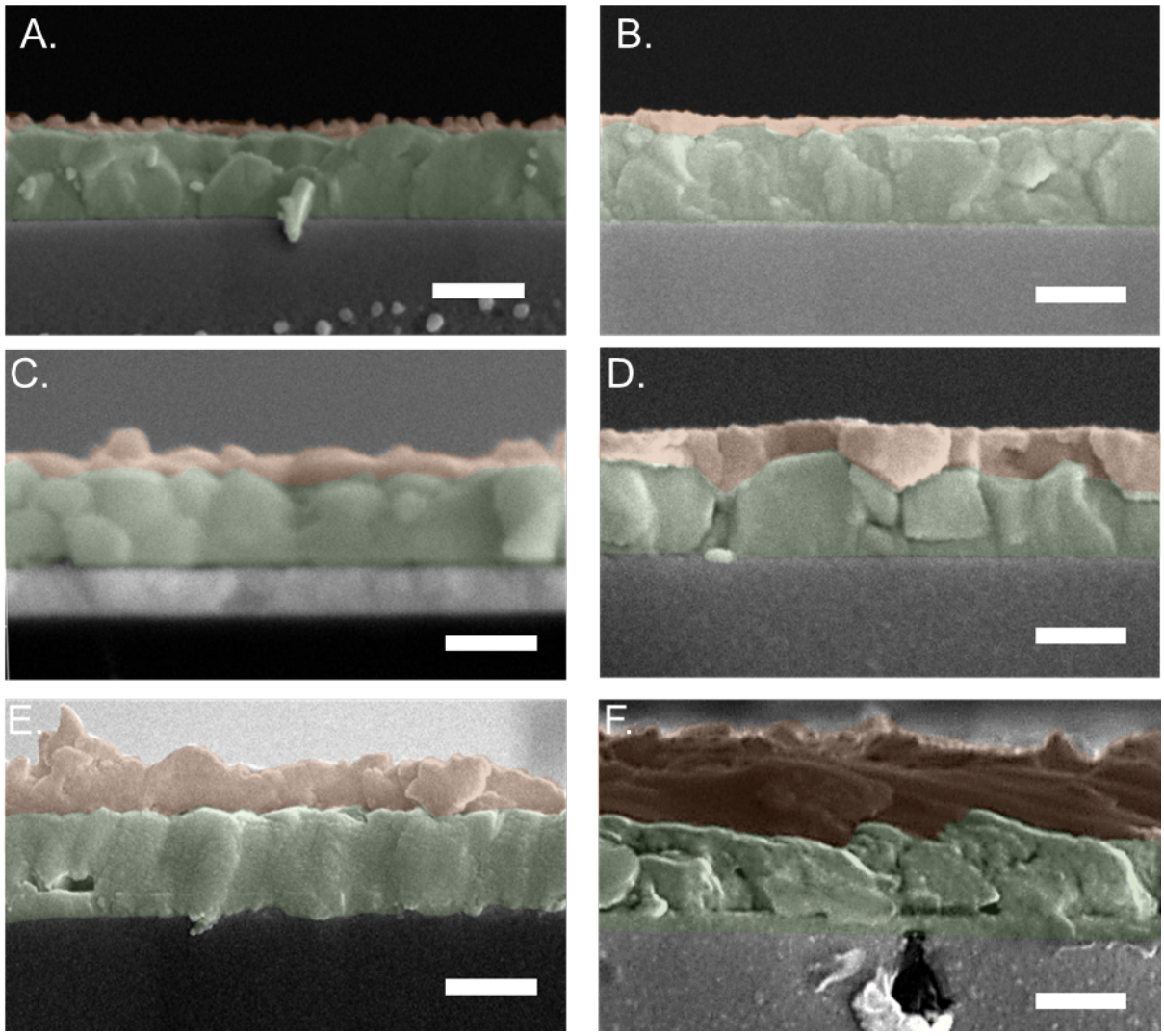

Figure S7. Cross-sectional scanning electron microscope images showing different thicknesses of the 2D perovskite layer grown on top of the 3D halide perovskite. The green shade represents 3D and the brown shade shows the 2D layer. The scale is 500 nm. The 2D perovskite layers (5-10 nm) less than the roughness of the underlying 3D layer do not form a continuous film.

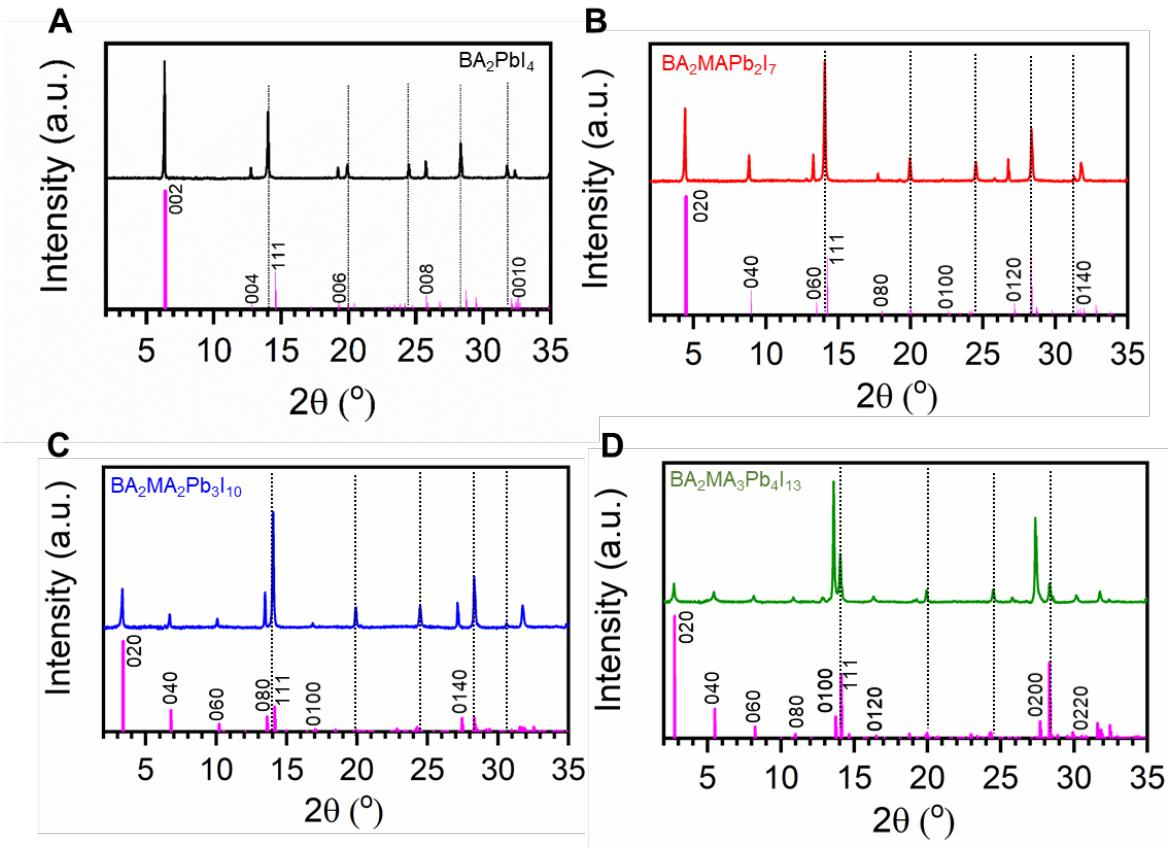

Figure S8. X-ray diffraction pattern from the 3D/PP-2D (n=1-4) HaP bilayer stack, compared with the simulated diffraction pattern of $BA_2MA_{n-1}Pb_nI_{3n+1}$ (n=1-4) obtained from crystallographic information file.

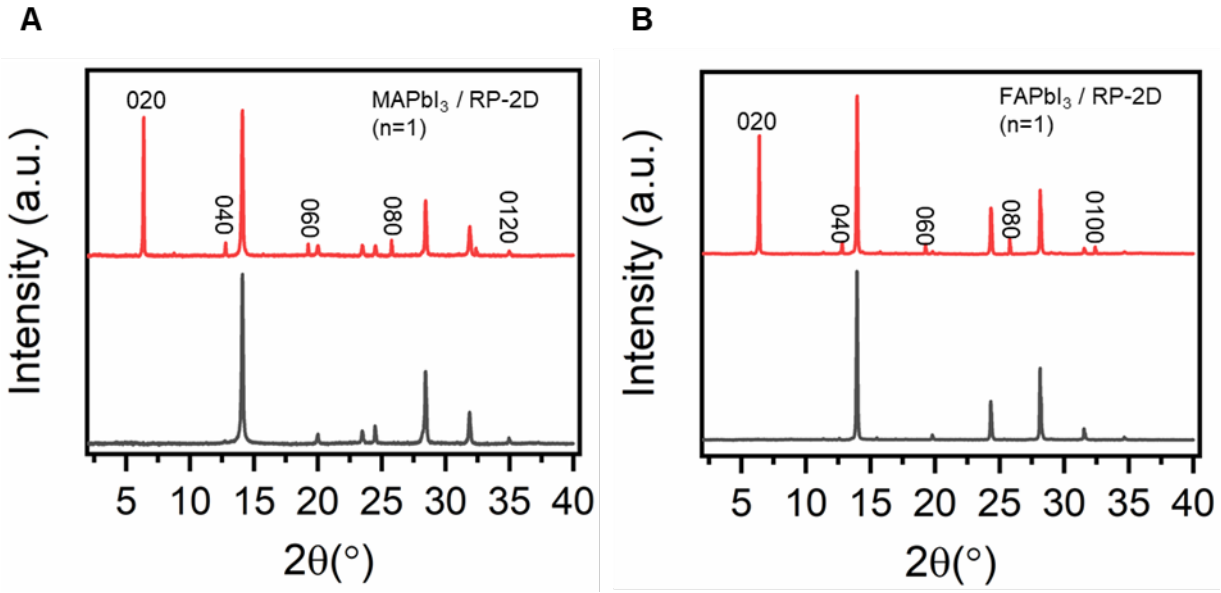

Figure S9. X-ray diffraction spectra of the $MAPbI_3$, and $FAPbI_3$ films without and with the 2D Ruddlesden popper perovskite, $(BA)_2PbI_4$.

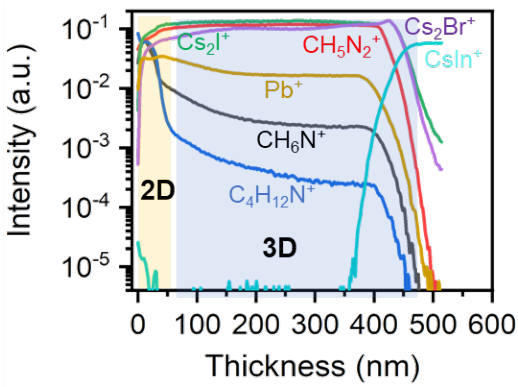

Figure S10. ToF-SIMS depth profile of the 3D/PP-2D ($BA_2MA_2Pb_3I_{10}$) HaP stack deposited on top of ITO shows the distribution of different ions across the thickness and the sharpness of the heterointerface.

Supplementary Note 3

Background of BA^+ molecular ion in the control-3D and 3D/2D bilayer stack TOF-SIMS measurements

ToF-SIMS characterizes elemental and molecular ions from the successively exposed surfaces over the sputtering. In the case of organic materials, the fragmentation of the molecular chain can induce different sub-fragments (children-like ions) or conserve longer molecular fragments such as a dimer, trimer, etc. (parent-like ions). During this process, some characteristic ions can be detected such as $C_4H_{12}N^+$ even when their corresponding compound (here, BA^+) is absent because of the recombination or the fragmentation of other molecular compounds (here, FA^+ and MA^+). However, the ion intensity of the characteristic ions such as $C_4H_{12}N^+$ is highly increased, by 3 orders of magnitudes in the 2D perovskite layer, when the corresponding compound is present (see Fig. 3B in MS, and Fig. S10).

The variation of the intensity after the 2D/3D interface as compared with the plateau of the intensity in the control sample is mainly due to the quality of the surface and the effect of the sputtering. The difference in crystallinity and chemical composition between the 2D and 3D layers can induce a difference in roughness due to the sputtering (see Fig. 3B in MS).

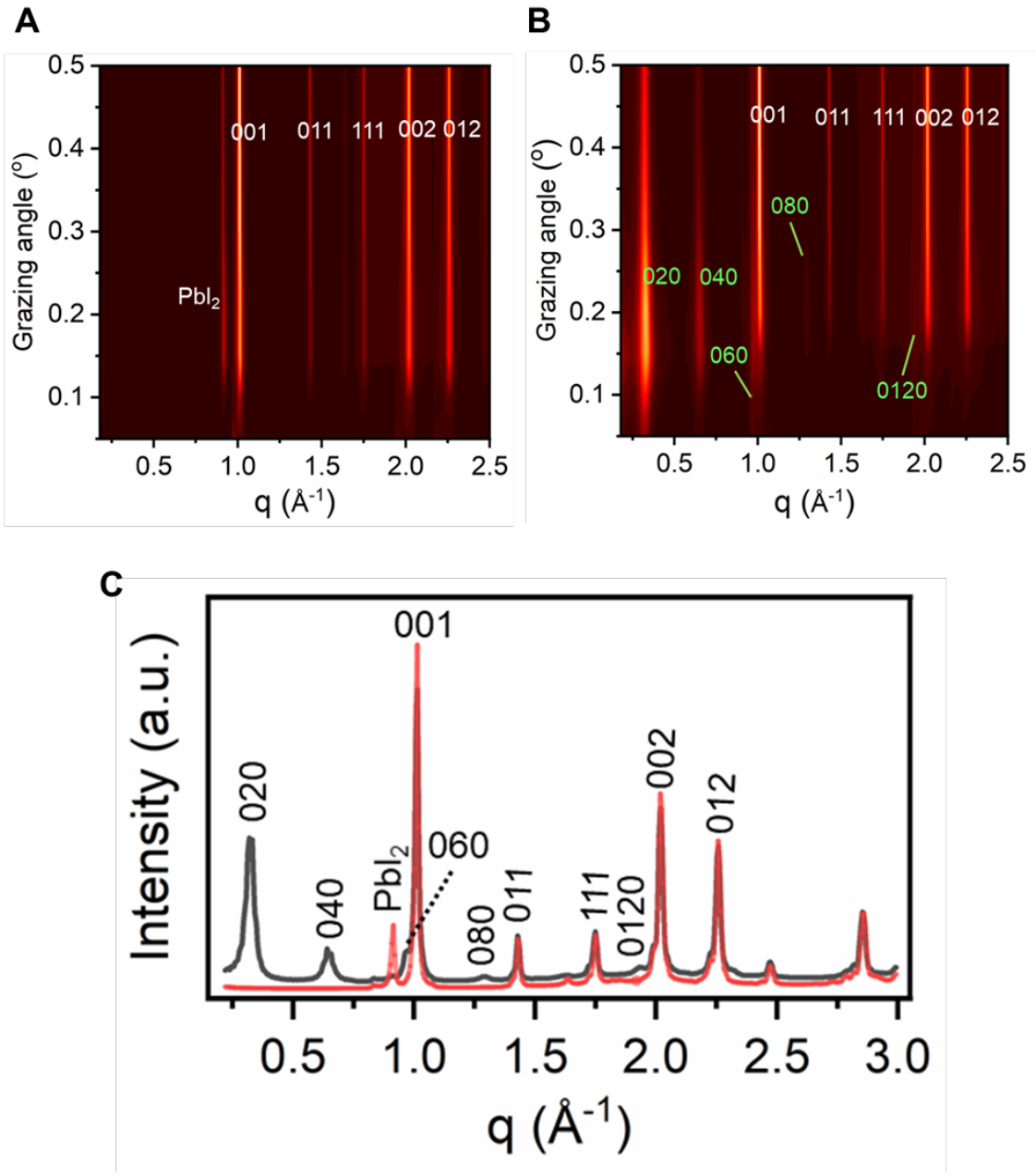

Figure S11. Evolution of the GIXRD peaks of A. 3D perovskite, and B. 3D/2D ($BA_2MAPb_2I_7$) film as a function of grazing angle of incidence, and C. Angular-integrated diffraction patterns of the 3D and 3D/2D ($BA_2MAPb_2I_7$) heterostructure thin films calculated from the 2D GIWAXS pattern measured at an incident angle of 0.20°.

Supplementary Note 4

We performed the grazing incident wide-angle scattering (GIWAXS) measurements at different incident angles (0 to 0.5°) to provide detailed evidence of the uniformity of $BA_2MA_2Pb_3I_{10}$ 2D perovskite layer grown on top of the 3D film and to probe the interface sharpness (see Figure 3C-D). Based on the calculated penetration depth curve for the 2D

Ruddlesden-popper perovskite (see Fig. 3E), the diffraction pattern measured at $\alpha = 0.1°$ shows surface features, and the diffraction pattern measured at $\alpha = 0.3°$ shows deeper bulk (>10 nm) features. The low incident angle ($\alpha = 0.08°$) GIWAXS pattern shows an oriented 2D RP n=2 diffraction pattern with no traces of 3D confirmed by the absence of diffraction rings (see Figure 3C). Furthermore, the diffraction pattern contains low angle diffraction peaks (< 1 $Å^{-1}$) which corresponds to the 2D perovskite stacking axis (0k0, k=2, 4, 6) planes. As we increase the incident angle ($\alpha = 0.15°, 0.50°$), the intensity of the 2D perovskite peak decreases followed by an increase in the intensity of rings corresponding to the 3D perovskite diffraction planes.

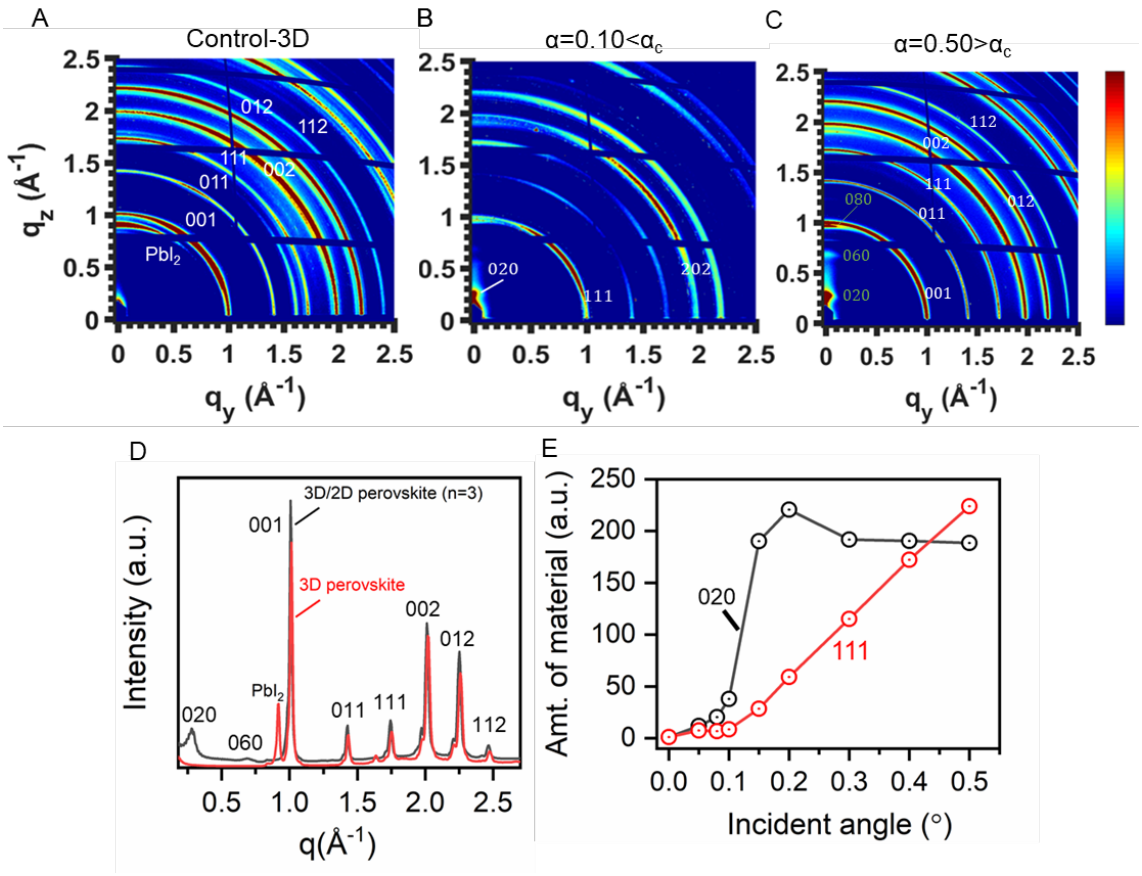

Figure S12. 2D GIWAXS pattern of the A. control 3D, and B-C. Angle dependent GIWAXS pattern of the 3D/PP-2D ($BA_2MAPb_2I_7$) HaP stack show evolution of 2D and 3D perovskites as we increase the incident angle, D. Angular-integrated diffraction patterns of the 3D and 3D/2D ($BA_2MA_2Pb_3I_{10}$) heterostructure thin films calculated from the 2D GIWAXS pattern measured at an incident angle of 0.20°, and E. Plot showing the variation in the amount of material of the 2D and the 3D perovskite extracted by the integrating the area under the (020) peak and (111) peak.

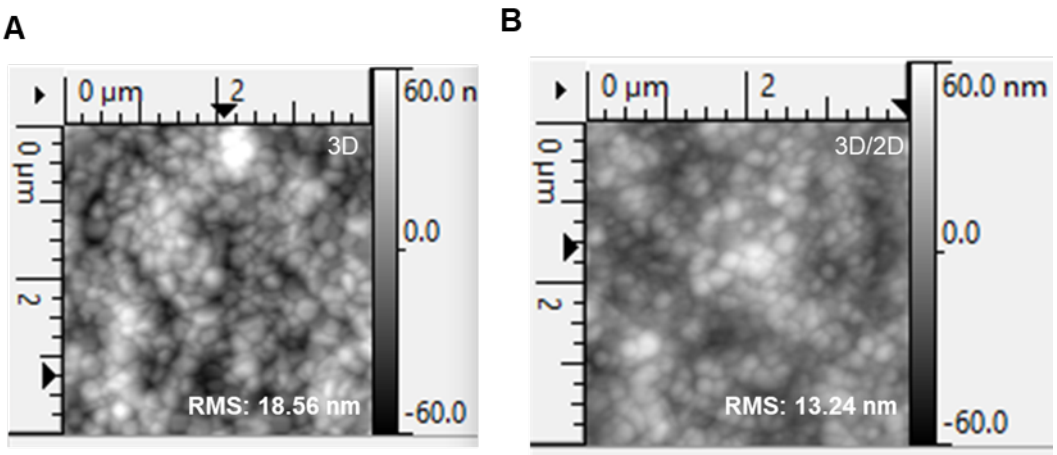

Figure S13. AFM image of the 3D control and 3D/2D perovskite showing the morphology and the extracted root mean square roughness.

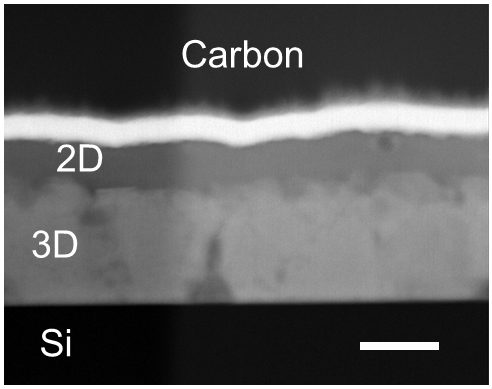

Figure S14. Cross-sectional dark-field HR-TEM image of the 3D/PP-2D ($BA_2MA_2Pb_3I_{10}$) HaP bilayer stack. The cracks within the 3D film are due to focused ion beam etching process. Scale bar 200 nm.

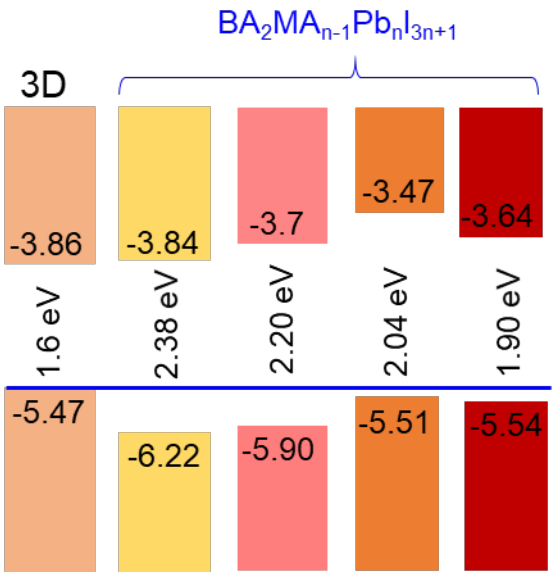

Figure S15. Plot showing predicted values of band energy levels of 2D, $BA_2MA_{n-1}Pb_nI_{3n+1}$ perovskites with different n-values (n=1-4), calculated using single-point calculations with GGA-PBE functional combined with DFT-1/2, including spin-orbit coupling.

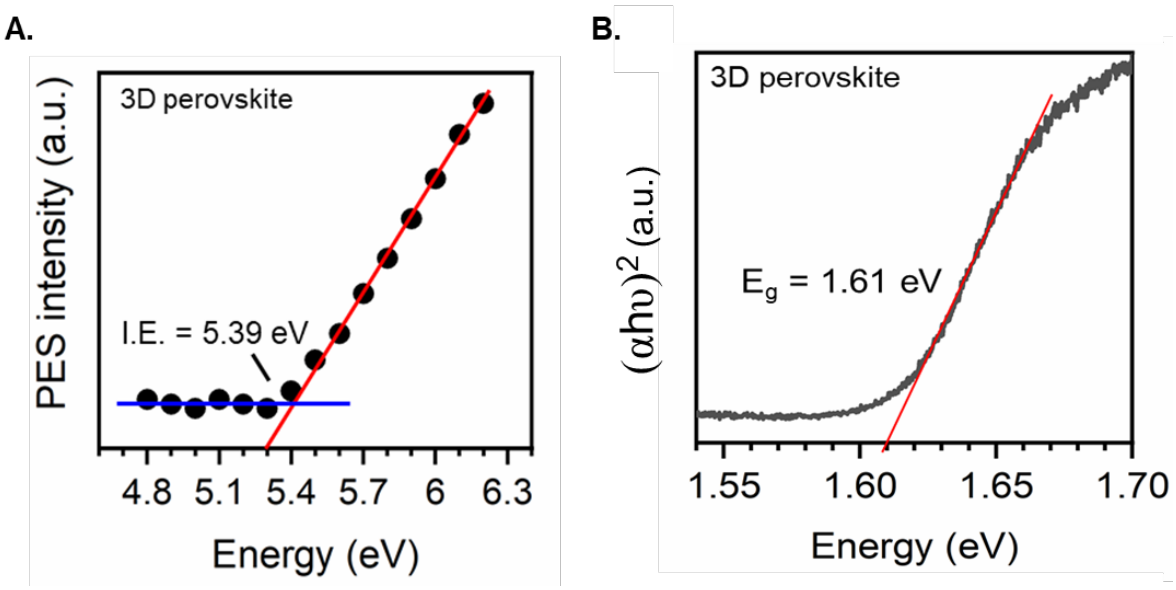

Figure S16. Plot showing the position of A. valence band maximum (VBM) with respect to the vacuum level (i.e., ionization energy [IE]) obtained by photoemission yield spectroscopy (PYS), and B. the tauc plot showing the bandgap extracted from the optical absorbance of the $Cs_5(MA_{0.10}FA_{0.90})_{95}Pb(I_{0.90}Br_{0.10})_3$ 3D HaP.

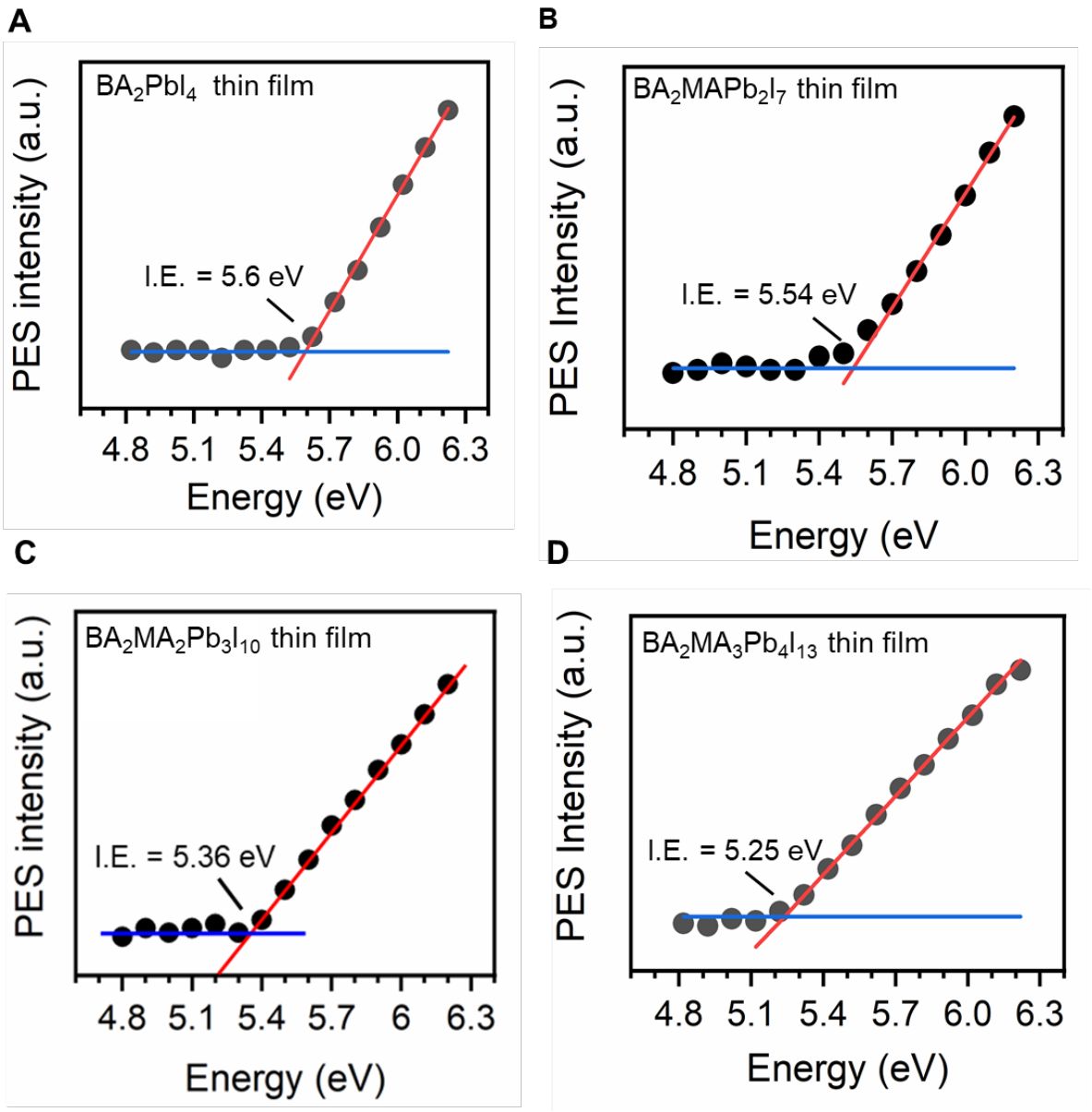

Figure S17. Plot showing the variation in the position of valence band maximum (VBM) with respect to the vacuum level (i.e., ionization energy [IE]) of the $BA_2MA_{n-1}Pb_nI_{3n+1}$ (n=1-4) 2D perovskite obtained by photoemission yield spectroscopy.

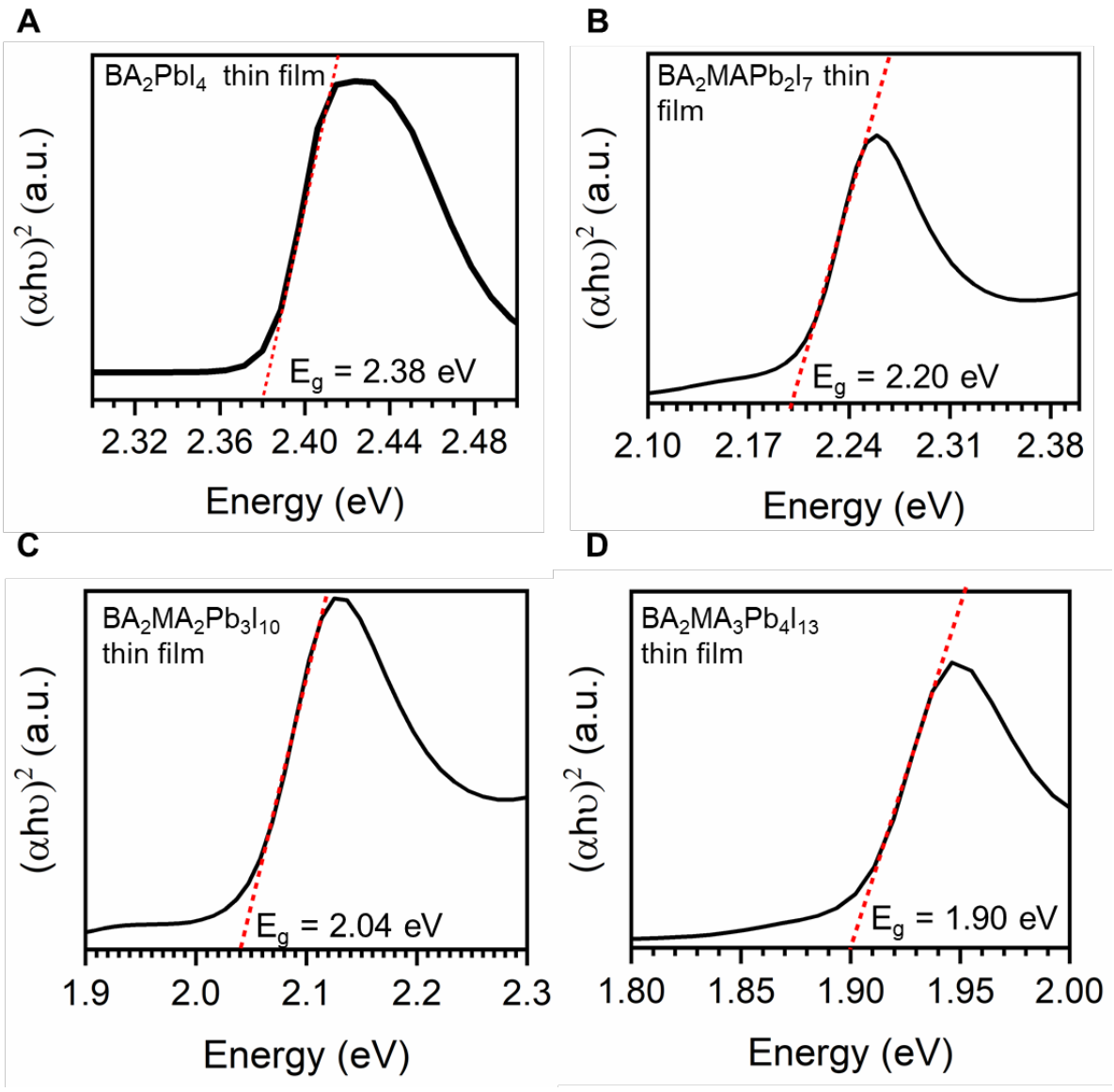

Figure S18. Tauc plot showing the bandgap (E_g) of the $BA_2MA_{n-1}Pb_nI_{3n+1}$ (n=1-4) 2D perovskite calculated from the optical absorbance of corresponding thin films.

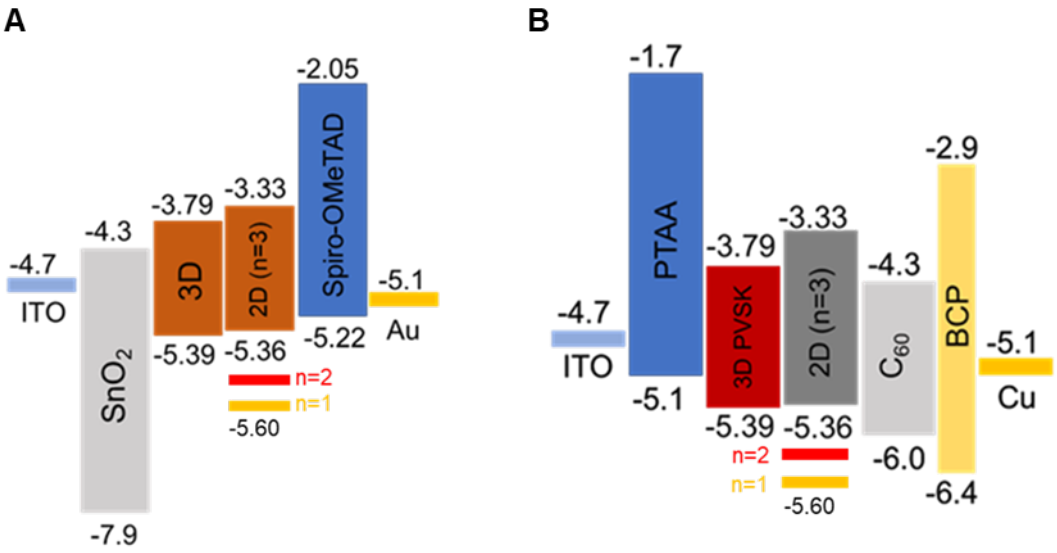

Figure S19. A. Energy level scheme of an n-i-p PSC with a 3D/PP-2D HaP bilayer as the active layer, showing the variation in VBM alignment of the 2D perovskite layer with different n-values (n≤3) deposited on the CsFAMA-3D control film, B. The energy level scheme of a p-i-n PSC with a 3D/PP-2D HaP bilayer as the active layer indicates the presence of a potential barrier for the extraction of electrons.

<u>Supplementary Note 5.</u> Reduced performance of the 3D/2D (n=1, n=2) n-i-p solar cell

We frabricated an n-i-p device with the architecture FTO/SnO_2/3D/PP-2D(n=3)/spiro-OMeTAD/Au, using 3D/2D (n=1, and n=2) bilayer stack. The resultant J-V curve are presented in Figure S20. We can clearly observe that, at lower thickness (<10 nm) of the 2D perovskite layer there is a slight increase in the performance of solar cell, followed by a drastic decrease due to the reduced short circuit current (J_{SC}) and fill factor (FF), indicating a barrier for charge transport within the solar cell.

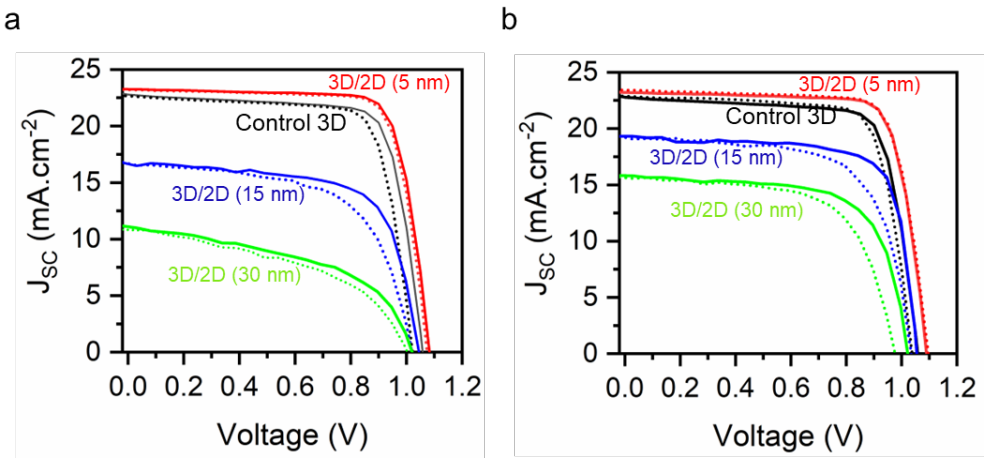

Figure S20. Current-voltage characteristics of the a) 3D/2D (BA_2PbI_4), b) 3D/2D ($BA_2MAPb_2I_7$) perovskite bilayer stack solar cell with varying 2D perovskite thickness.

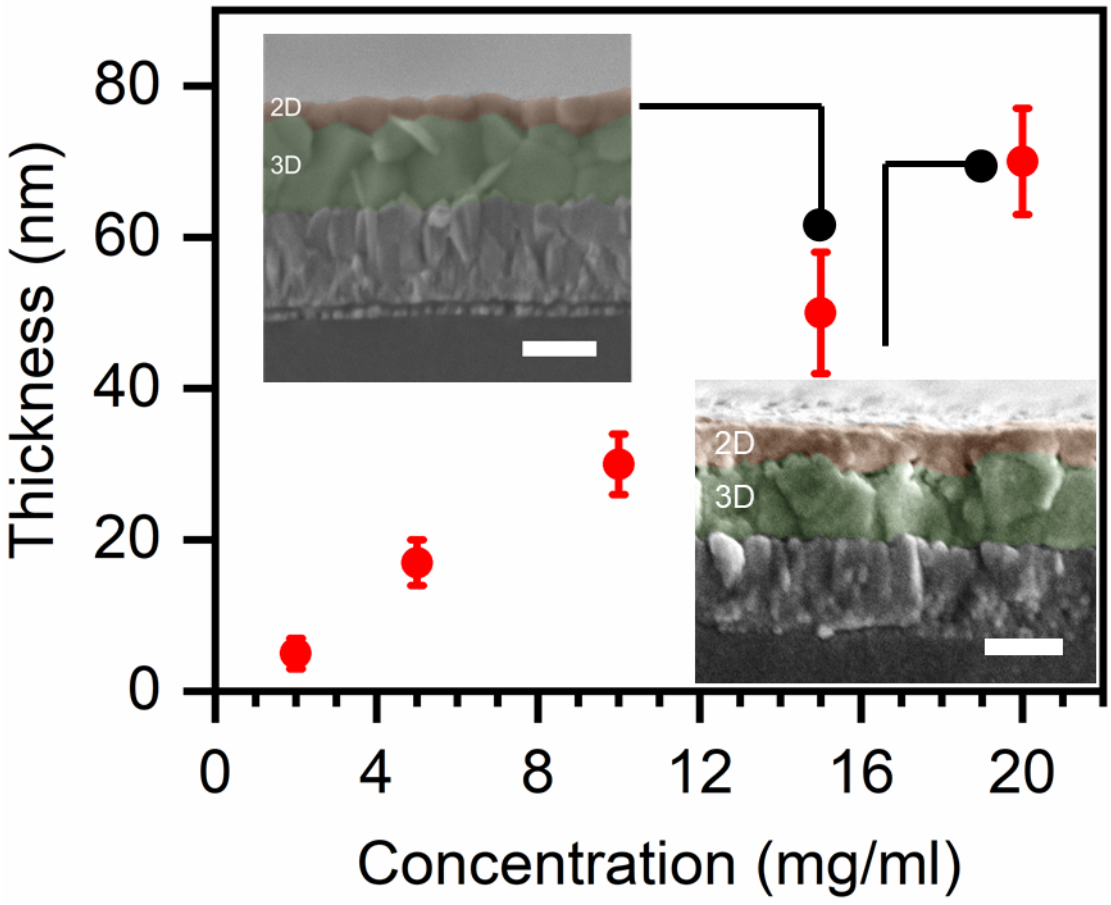

Figure S21. Plot showing the variation in thickness of the 2D $BA_2MA_2Pb_3I_{10}$ perovskite layer spin-coated on top of the 3D film. The scale is 500 nm.

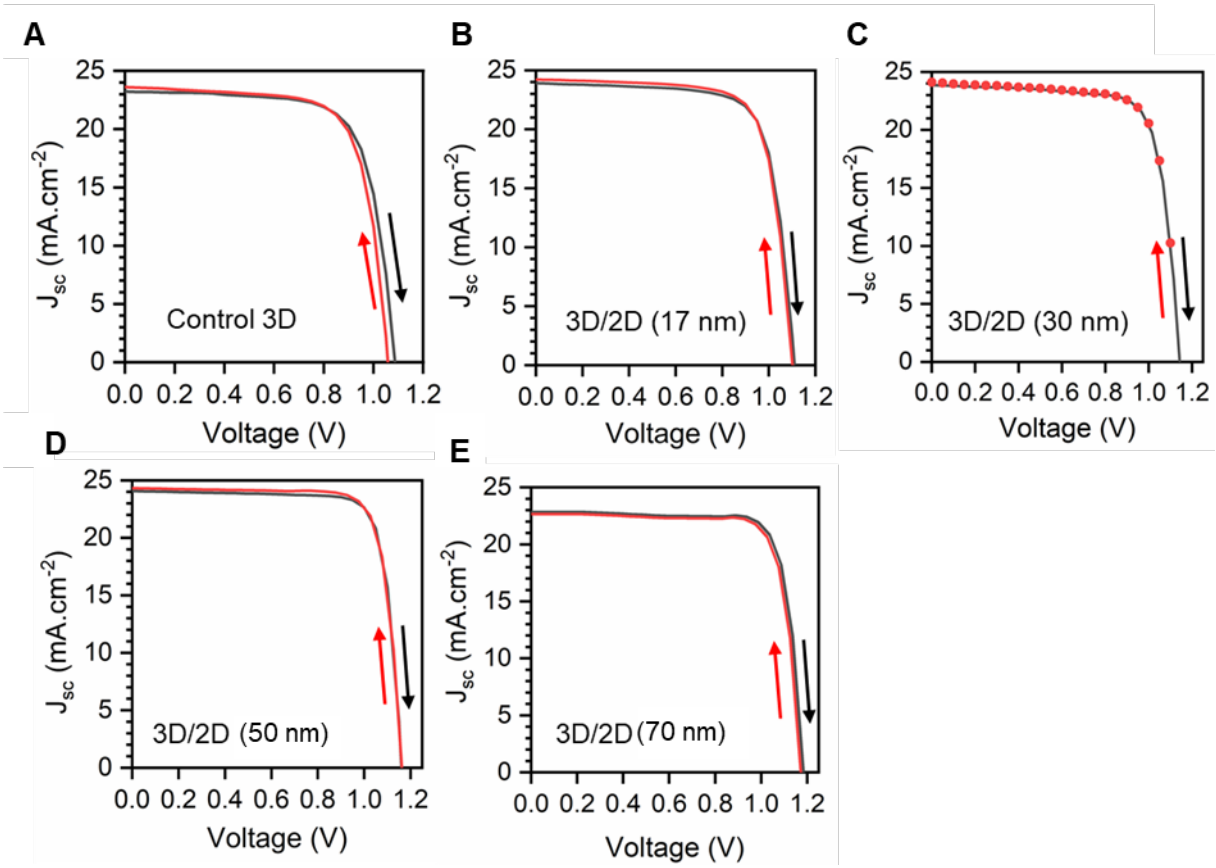

Figure S22. Plot showing the current-voltage characteristics of the 3D/PP-2D perovskite solar cells without and with different thicknesses of $BA_2MA_2Pb_3I_{10}$ 2D perovskite layer measured under forward and reverse scan to verify the hysteresis.

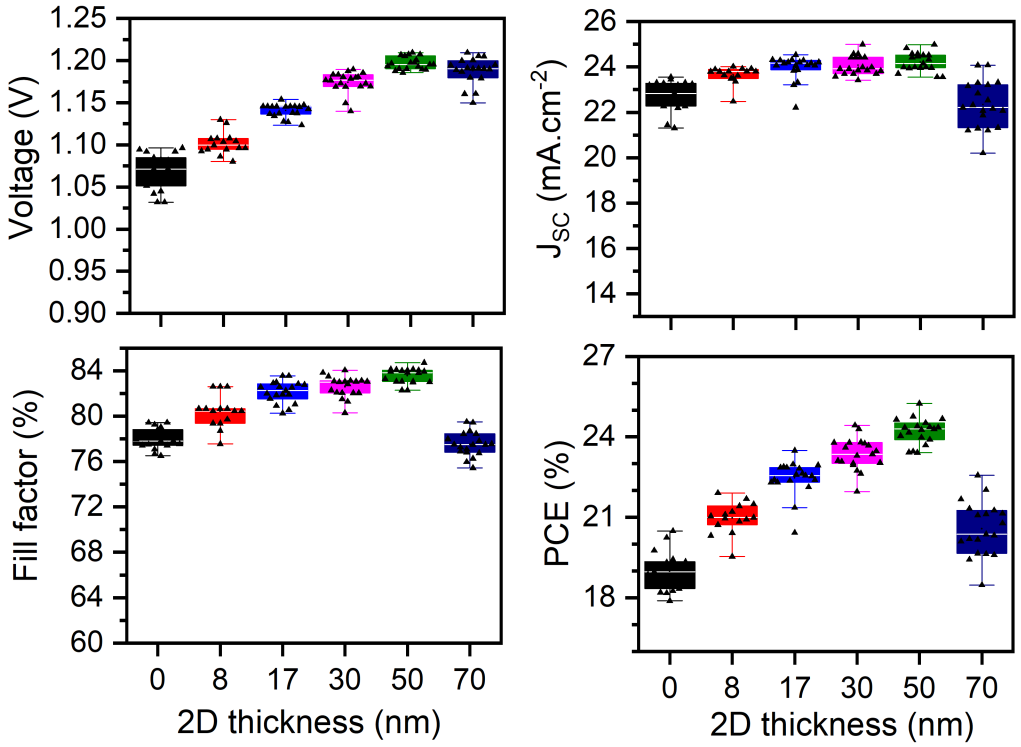

Figure S23. Statistics of the PV parameters of 3D/2D HaP bilayer n-i-p device with different thicknesses of the overlying 2D $BA_2MA_2Pb_3I_{10}$ layer.

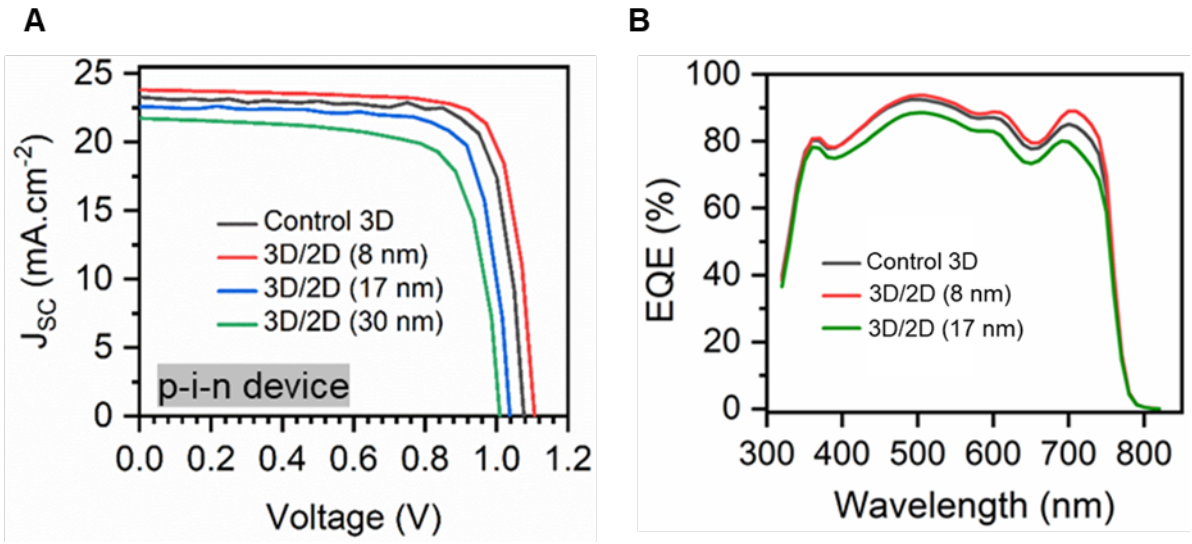

Figure S24. A. Current-voltage characteristics, and EQE characteristics of the champion 3D/PP-2D ($BA_2MA_2Pb_3I_{10}$) HaP bilayer p-i-n devices as a function of the 2D layer thickness**.**

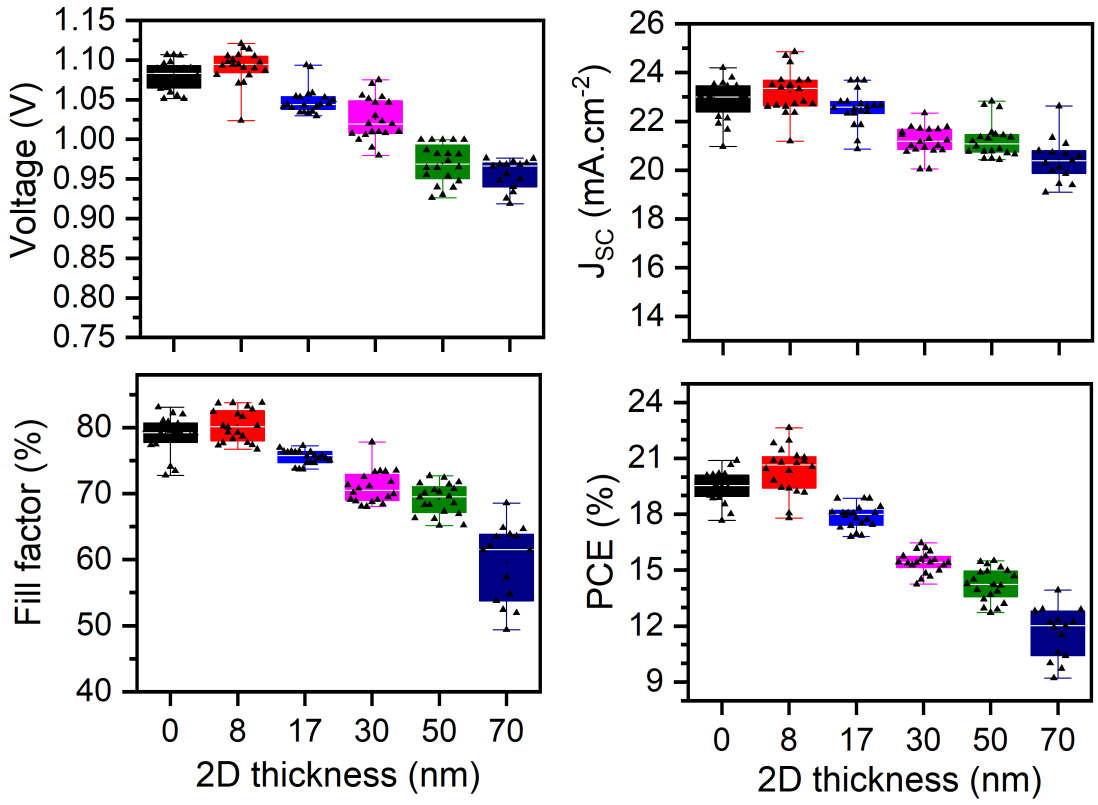

Figure S25. Statistics of the PV parameters of 3D/2D HaP bilayer p-i-n device with different thicknesses of the overlying 2D $BA_2MA_2Pb_3I_{10}$ layer.

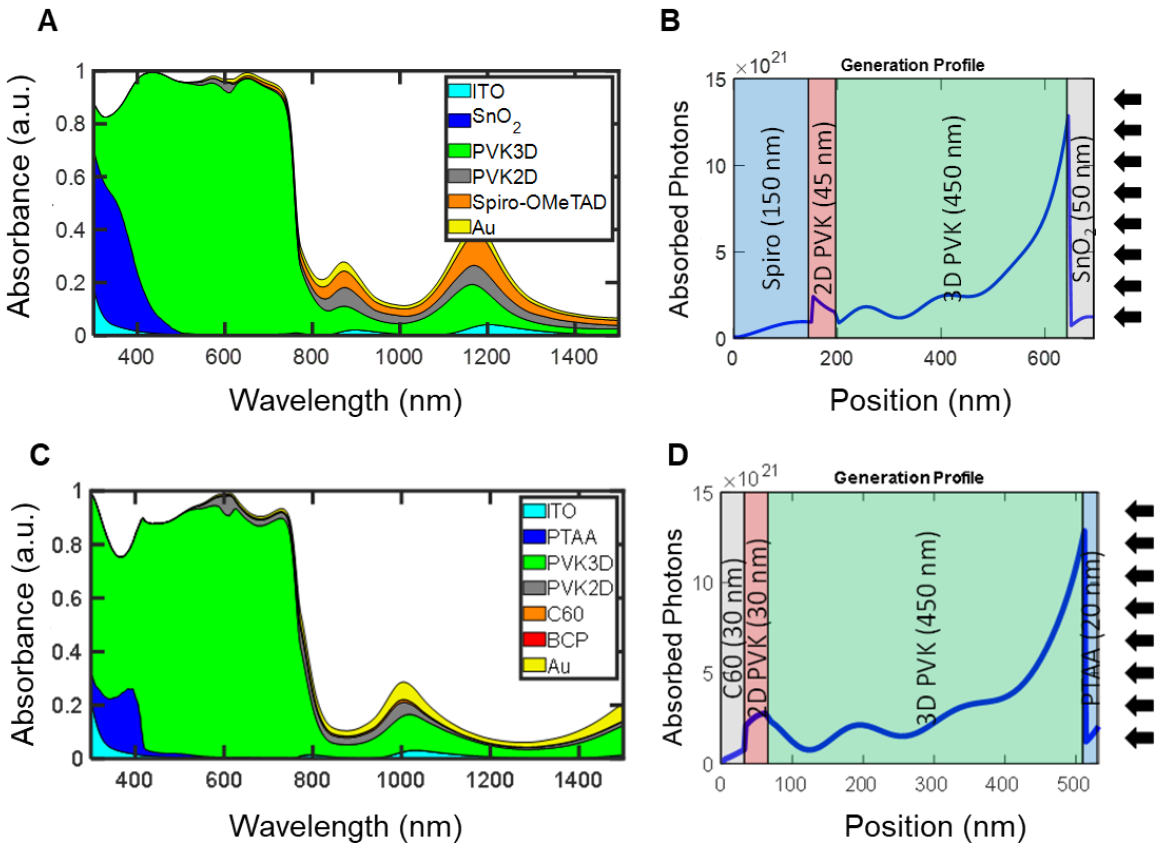

Figure S26. A. Absorbance as a function of wavelength and B. photogeneration profile at different layers for an n-i-p device architecture. The black arrows show the direction of the incident light. The contacts are not shown in photogeneration, C. Absorbance as a function of wavelength, and D. photogeneration profile at different layers for a p-i-n device. The black arrows indicate the direction of the incident light. The contacts are not shown in photogeneration.

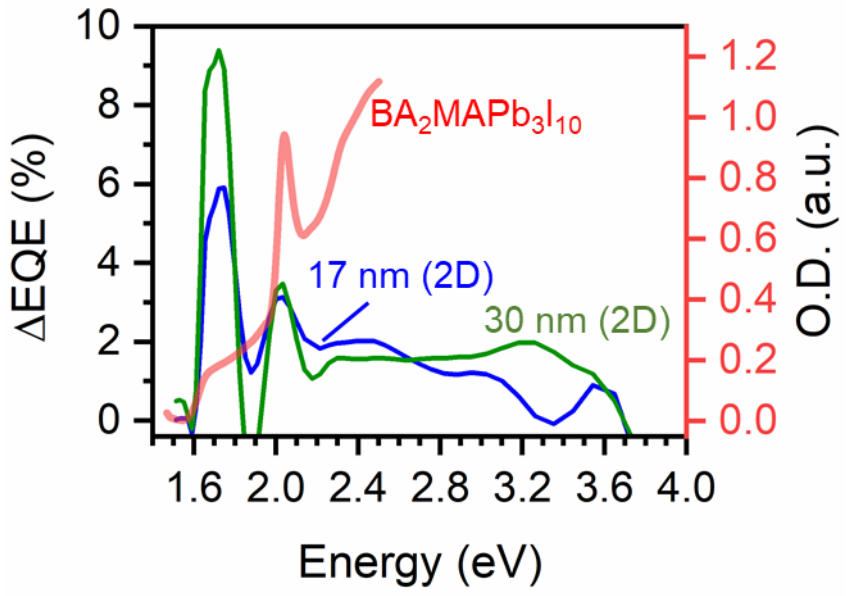

Figure S27. Plot showing the ΔEQE curve obtained by subtracting the EQE of the devices without and with the overlying $BA_2MA_2Pb_3I_{10}$ 2D perovskite layer of different thicknesses.

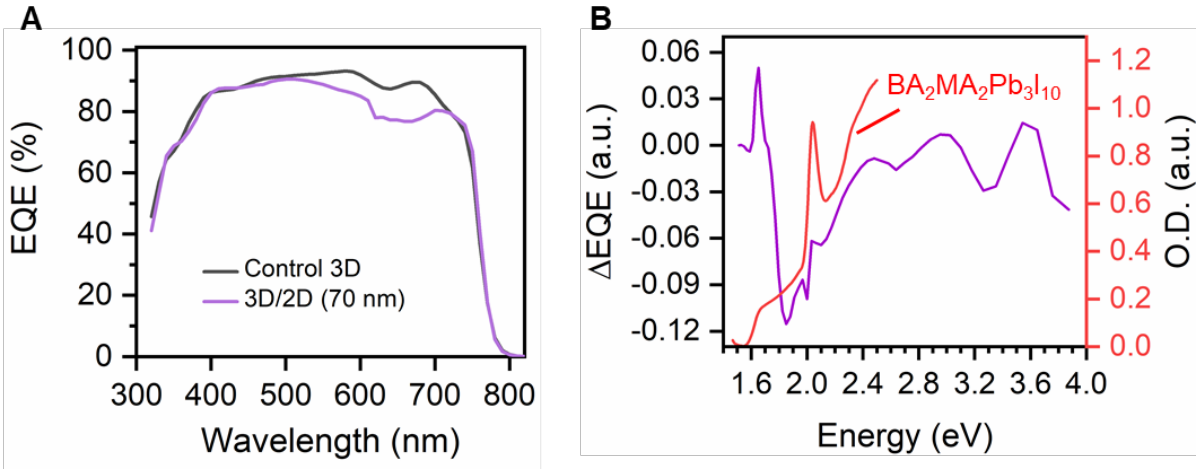

Figure S28. Plot showing the A. EQE spectrum of the control 3D, 3D/2D heterostructure, and B. the ΔEQE curve obtained by subtracting the EQE of the devices without and with the overlying $BA_2MA_2Pb_3I_{10}$ 2D perovskite layer with a thickness of ~70 nm.

Supplementary Note 6

To elucidate the contribution of 2D perovskite on the J_{SC}, we evaluated the difference in EQE (ΔEQE) of the 3D/2D and the control 3D device for different thicknesses and compared it with the 3D/2D (n=3) absorption (see Fig. S27). We observed enhanced photoresponse features across the 3D perovskite band edge (□1.6 eV), and at the excitonic absorption of the n=3 2D perovskite (□2.0 eV). These features became stronger with the increase in the thickness of the overlying 2D perovskite layer indicating the

photogeneration nature of the 2D, *n*=3 layer. However, for a thickness of □70 nm, the photoresponse decreases (see Fig. S28); depicted by the negative response of the ΔEQE plot, which shows an abrupt decrease in the region around the excitonic absorption of the 2D perovskite (n=3), followed by a uniform decrease in other wavelength regions indicating enhanced charge carrier recombination in the 2D layer.

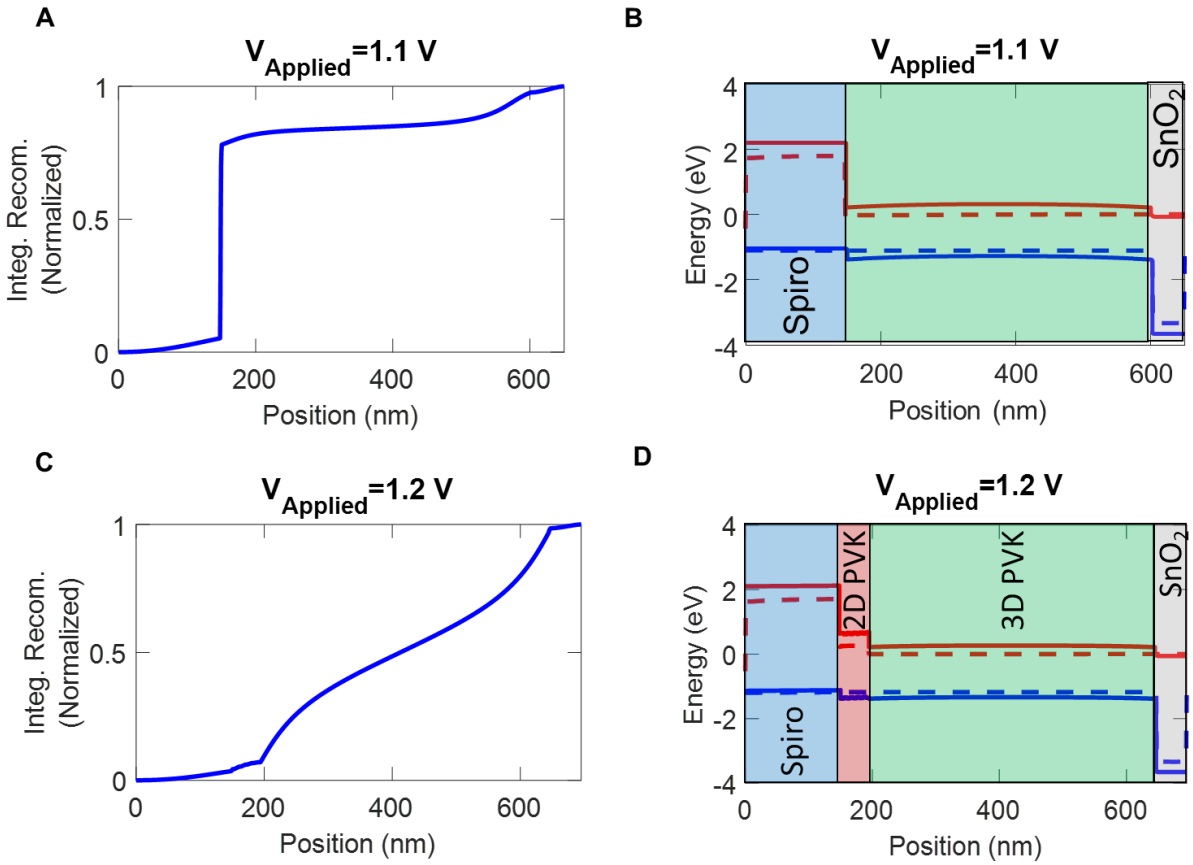

Figure S29. Plot depicting the integrated normalized recombination of the 3D/2D HaP bilayer n-i-p device A. without and C. with 50 nm of 2D HaP layer showing that the 2D perovskite layer prevents the recombination close to the V_{oc} of the two devices. The energy band diagram of B. without and D. with 50 nm of the 2D HaP layer shows that the higher bandgap of the 2D perovskite layer lowers the available charged carriers for recombination to occur at the 2D perovskite and spiro-OMeTAD interface.

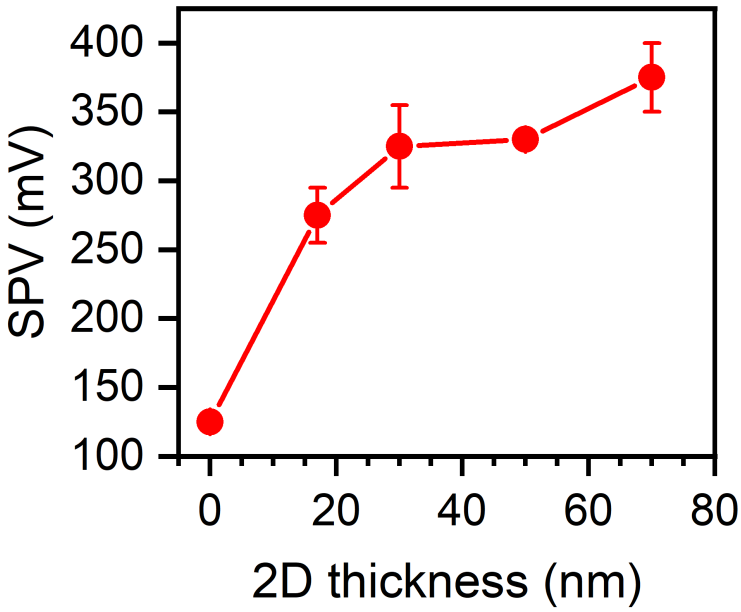

Figure S30. Surface photovoltage as a function of 2D layer thickness. The SPV shows a general increase from the control (0 mg), with the thickest layer always showing the largest SPV. Error bars represent the distribution of SPV measured at several areas on the surface.

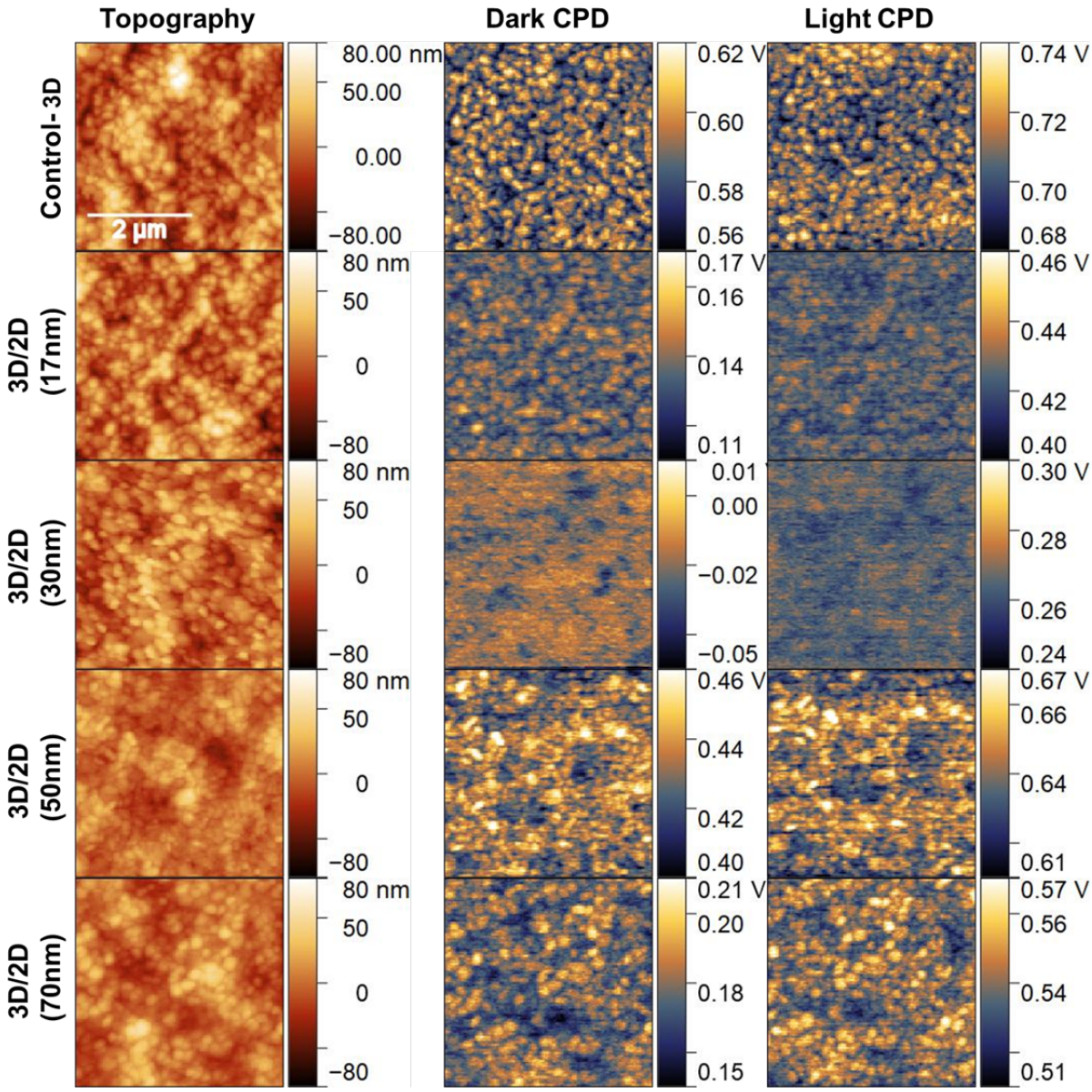

Figure S31. Representative images showing the AFM topography, and contact potential difference (CPD) in the dark and under illumination (590 nm, ~2.4 mW/cm^2) for different 2D thicknesses.

Supplementary Note 6.

According to the Shockley equation, the V_{OC} is given by

$$V_{oc} = \frac{nk_BT}{q} ln\left(\frac{J_{sc}}{J_O}\right)$$

where where n is the ideality factor of the diode which is in the range of 1−2, kB is the Boltzmann constant, T is the absolute temperature, q is the elementary charge, J_{sc} is the photo-generated short-circuit current density, and J_o is the reverse saturation current density. There are no big difference in the J_{sc} of the solar cell, and hence

the V_{oc} is largely dependent on the magnitude of J_o The increase in J_o results in a decrease in V_{oc} and vice versa.

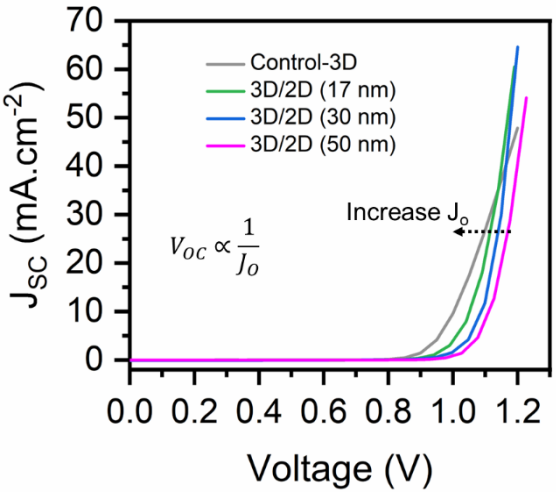

Figure S32. Dark current-voltage traces of the 3D/PP-2D ($BA_2MA_2Pb_3I_{10}$) n-i-p PSCs as a function of the 2D layer thickness obtained by spin coating different concentration of the 2D perovskite solution in MeCN.

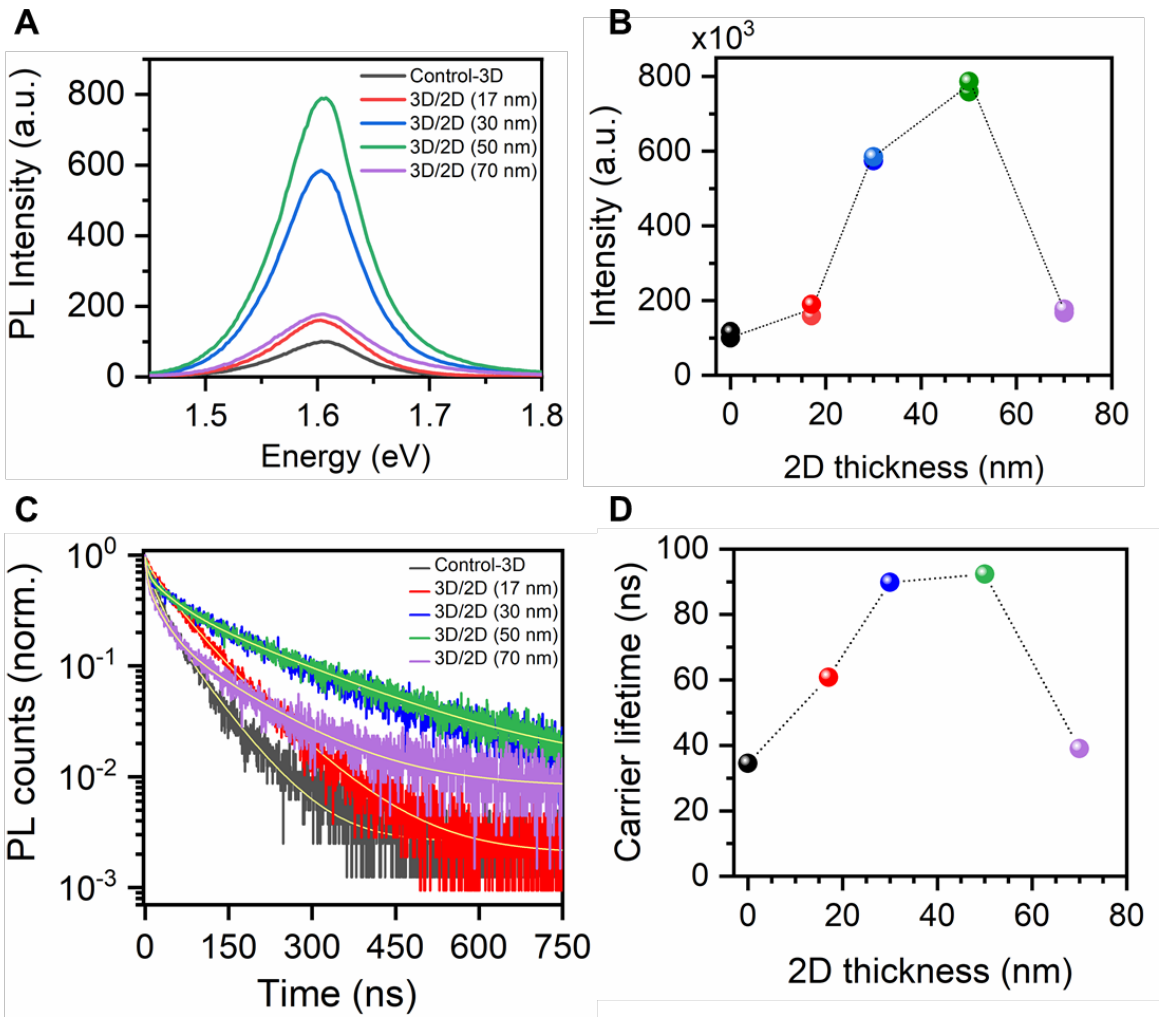

Figure S33. Plots showing A. the steady-state photoluminescence, B. change in the PL intensity, C. time-resolved PL decay curves, and C. change in carrier lifetimes of 3D perovskite film without and with different thicknesses of overlaying 2D $BA_2MA_2Pb_3I_{10}$ perovskite layer fabricated on top of ITO/SnO_2 substrate.